

# The shape distribution of superclusters in SDSS DR12

Satadru Bag,<sup>1\*</sup> Lauri Juhan Liivamägi,<sup>2†</sup> Maret Einasto<sup>2</sup>

<sup>1</sup> *Korea Astronomy and Space Science Institute, Daejeon 34055, Korea*

<sup>2</sup> *Tartu Observatory, University of Tartu, Observatooriumi 1, 61602 Tõravere, Estonia*

## ABSTRACT

Galaxy superclusters, the largest galaxy structures in the cosmic web, are formed due to the gravitational collapse (although they are not usually gravitationally bound). Their geometrical properties can shed light on the structure formation process on cosmological scales, hence on the fundamental properties of gravity itself. In this work we study the distributions of the shape, topology and morphology of the superclusters extracted from Sloan Digital Sky Survey Data Release 12 (SDSS DR12) main galaxy sample and defined in two different ways – using fixed and adaptive density threshold in the luminosity-density field. To assess the geometry and topology of each individual supercluster, we employ Minkowski functionals and Shapefinders, precisely calculated by the shape diagnostic tool SURFGEN2. Both supercluster samples produce similar shape distributions. Perhaps not surprisingly, most superclusters are spherical in shape with trivial topology. However, large superclusters with volumes  $V \gtrsim 10^4$  Mpc<sup>3</sup> are statistically found to be filamentary with non-zero genus values. The results, supercluster catalogues and shape distributions are publicly available.

**Key words:** large-scale structure of Universe

## 1 INTRODUCTION

The large-scale distribution of matter in the Universe is the result of collapse of small initial Gaussian fluctuations in density (see e.g. Davis et al. 1985; Sahni & Coles 1995; Bernardeau et al. 2002; Springel et al. 2005; Springel et al. 2006). Nonlinear gravitational amplification converts these isotropic random fluctuations into a field with striking geometrical structure: empty 3-dimensional voids bounded by 2-dimensional sheets, which intersect in filaments, with the filaments joining at nodes forming clusters (e.g. Jõeveer et al. 1978; Gregory & Thompson 1978; Zeldovich et al. 1982; Einasto et al. 1984; de Lapparent et al. 1986; Melott 1990; Bond et al. 1996; Sathyaprakash et al. 1996; Bond et al. 2010; Jasche et al. 2015). The study of this ‘cosmic web’ is important in modern cosmology. The history of galaxy formation in different regions of the web have been affected in different ways, giving different observational tests for models for the assembly of galaxies. On a more general scale, the cosmic web can be used to test the models for gravity and cosmology pertaining to both linear and non-linear structure formation.

The largest structures in the cosmic web are galaxy superclusters, overdensity regions which consist of galaxy groups and clusters, connected by filaments. Superclusters play a key role in understanding the properties and evolution of the cosmic web. Examples of rich superclusters that have been studied in detail in literature include, for example, the Shapley

supercluster (Shapley 1930), the Corona Borealis supercluster (Einasto et al. 2021b, and references therein), Laniakea supercluster (Tully et al. 2014), the supercluster SC1 A2142 (Einasto et al. 2015), and the Saraswati supercluster (Bagchi et al. 2017), etc. In some cases, rich superclusters are close together and form supercluster complexes, as the Sloan Great Wall (Vogeley et al. 2004; Einasto et al. 2016) and the BOSS Great Wall (Lietzen et al. 2016; Einasto et al. 2022). Superclusters can be defined in a different ways, recently briefly reviewed by Einasto et al. (2020).

In the present study we adopt the traditional definition of superclusters as high-density regions in the cosmic web. We use galaxy data from the Sloan Digital Sky Survey (SDSS) to calculate the luminosity-density field and define connected high-density regions in this field as galaxy superclusters. With this method the choice of the density level to determine superclusters is important. We use two approaches for that. One way is to use fixed threshold luminosity-density limit. At low threshold density superclusters merge to form very large connected systems, and at very high threshold density only the highest density cores belong to superclusters. Einasto et al. (2011a) proposed that, using data on superclusters from the richest galaxy system in the nearby Universe, the Sloan Great Wall, the threshold density to define individual superclusters should be close to  $D_{\text{th}} = 5.0$  in the units of mean density. We apply this threshold density also in the present paper. Another way to choose the density level for is to find the threshold value for each supercluster individually, based on the density distribution around the location of a supercluster. We describe this method in detail below.

\* satadru@kasi.re.kr

† juhan.liivamagi@ut.ee

The large-scale structure datasets are analysed using numerous statistics, as recently reviewed in [Libeskind et al. \(2018\)](#), however the focus has been on the correlation statistics. With the major advances in the cutting-edge optical and radio surveys in recent years, well complemented by the recent progresses in large-scale simulations, it has now become extremely important to look beyond the simplest 2-point correlation statistics (or power spectrum) and search for methods which can extract more information out of the persistently growing datasets. However, the higher order functions can be difficult to calculate, and sometimes they face conceptual challenges. In this context, the Minkowski functionals (MFs) provide a robust and powerful means of studying the morphology of the large-scale structure of the Universe. They implicitly contain information from all of the N-point correlation functions and play a role that is complementary to that of the correlation statistics in probing the gravity at non-linear cosmological scales. In view of the upcoming spectroscopic and photometric surveys like DESI, LSST, the importance of MFs in analysing large-scale structure datasets is expected to grow rapidly in the near future. Since MFs were introduced in cosmology by [Mecke et al. \(1994\)](#), they have been frequently employed to study the morphology of the cosmic web ([Schmalzing & Buchert 1997](#); [Sahni et al. 1998](#); [Sathyaprakash et al. 1998](#); [Hikage et al. 2003](#); [Einasto et al. 2007, 2011c](#); [Pratten & Munshi 2012](#); [Wiegand et al. 2014](#); [Wiegand & Eisenstein 2017](#); [Matsubara & Kuriki 2020](#); [Matsubara et al. 2020](#); [Lippich & S'anchez 2020](#); [Appleby et al. 2021](#)), the cosmic reionization process ([Friedrich et al. 2011](#); [Yoshiura et al. 2017](#); [Bag et al. 2018](#); [Chen et al. 2019](#); [Kapahtia et al. 2021](#); [Pathak et al. 2022](#)), as well as the cosmic-microwave background (CMB) ([Schmalzing & Gorski 1998](#); [Novikov et al. 1999, 2000](#); [Hikage et al. 2006](#)). With few exceptions, these studies calculate ‘global’ MFs of the whole isodensity surface.

In this paper our approach has two important differences from the majority of the previous studies of MFs in the literature. First, instead of studying the global MFs of the whole volume, we explore the morphology in terms of ‘shape’ of the individual superclusters. Previously, a number of studies explored the morphology and evolution of a small number of superclusters ([Einasto et al. 2007, 2011b, 2014, 2019, 2021a](#)). Our present study extends morphology analysis of superclusters, for the first time, to a large dataset. Secondly, instead of focusing on just MFs, in this work we study their ratios which are introduced as ‘Shapefinders’ by [Sahni et al. \(1998\)](#). The Shapefinders provide us with the measure of the three physical dimensions of an object (thickness, width, and length of a cluster or void or, in our case, of a supercluster). Our main method of analysis shall be the computationally advanced version of the SURFGEN algorithm ([Sheth et al. 2003](#); [Sheth 2006](#)). This algorithm provides means of determining the geometrical and topological properties of isodensity contours delineating superclusters and voids within the cosmic web ([Sheth 2004](#); [Shandarin et al. 2004](#)). We apply SURFGEN2 algorithm which models the surfaces of the clusters and voids through the advanced ‘Marching Cube 33’ triangulation scheme ([Chernyaev 1987](#); [Lorensen & Cline 1995](#)). Its accuracy in determining MFs and Shapefinders is much better than the traditional methods ([Schmalzing & Buchert 1997](#)), such as the techniques based on Crofton’s formula ([Crofton 1868](#)), Koenderink’s invariant ([Koenderink 1984](#)) or

germ-grain models ([Mecke et al. 1994](#); [Schmalzing et al. 1996](#); [Wiegand et al. 2014](#)).

The paper is organised as follows. Section 2 describes how we construct the density field using the observed galaxies in SDSS DR12. Next, in Section 3 we study the density field using percolation and define the superclusters using isodensity surfaces. A brief overview of MFs and Shapefinders (as well as the code SURFGEN2) is provided in Section 4. We present our main result in Section 5 where we study the shape of superclusters defined using two approaches: using a globally fixed or flat density threshold and with individual thresholds set using an adaptive mechanism. We summarise our results and conclude in Section 6. Throughout this paper, we assume the cosmological parameters provided in [Planck Collaboration et al. \(2016\)](#): the Hubble constant  $H_0 = 67.8 \text{ km s}^{-1} \text{ Mpc}^{-1}$ , the matter density  $\Omega_m = 0.308$ , and the dark energy density  $\Omega_\Lambda = 0.692$ .

## 2 SDSS DR12 MAIN GALAXY SAMPLE AND CONSTRUCTING THE LUMINOSITY DENSITY FIELD

### 2.1 Galaxy data

Galaxy superclusters in this study are based on the main contiguous area sample from SDSS DR12, the so-called Legacy Survey ([Eisenstein et al. 2011](#); [Alam et al. 2015](#)). Galaxy data in the more recent SDSS data release 16 is virtually unchanged compared to the DR12 in the Legacy Survey area ([Ahumada et al. 2020](#)). Specifically, we use the value added catalogue of galaxies, groups and clusters by [Tempel et al. \(2017\)](#). The galaxy sample is volume-limited and consists of 584 449 galaxies with spectroscopic redshifts up to  $z = 0.2$  and brighter than the Petrosian  $r$ -band magnitude 17.77. The catalogue also contains 88 662 galaxy groups with a minimum of two members, assembled using a modified friend-of-friend (FoF) method with a variable linking length. Details about compiling the galaxy sample are given in [Tempel et al. \(2014\)](#) and [Tempel et al. \(2017\)](#).

### 2.2 Luminosity density fields

The density field from the SDSS DR12 main galaxy sample was constructed closely following [Liivamägi \(2017\)](#); [Liivamägi et al. \(2012\)](#). In short, galaxy luminosities are interpolated onto a regular Cartesian grid with a three-dimensional smoothing kernel.

We use two properties given in the [Tempel et al. \(2017\)](#) galaxy catalogue to reduce observational effects on the density field. First, we use the ‘corrected’ distance, which takes into account the velocity dispersion in groups and clusters suppressing the cluster-finger (finger-of-god) redshift distortions ([Kaiser 1987](#)). This correction, of course, is only statistical and not applicable to determine the positions of individual galaxies, however, one can make an assumption that clusters and groups should be more or less spherical and not strongly elongated along the line of sight.

Another important issue is that the number of galaxies in volume-limited samples decreases with distance due to only brighter objects being observed. In order to counter that, galaxy luminosities are weighted before interpolation, this

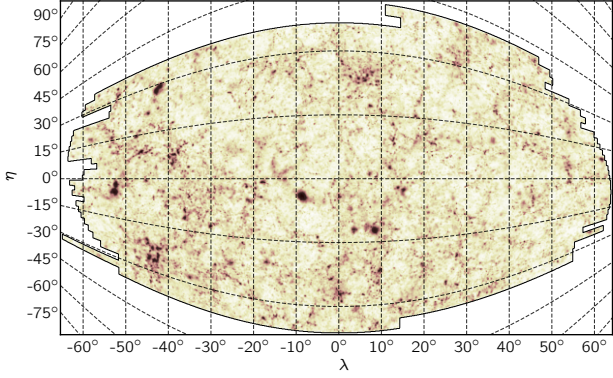


**Figure 1.** Sky projection of the density field of the SDSS DR12 main galaxy sample in survey coordinates  $\lambda$  and  $\eta$ . Black lines show the outline of the mask.

compensates for the amount of unobserved luminosity, i.e. galaxies that fall outside the observational magnitude limits. The weight is calculated as the ratio between the area under full galaxy luminosity function and the fraction that is inside the survey visibility window at the distance of the galaxy. As with the cluster-finger suppression, doing this is correct only in a statistical sense. In this work, we are looking at structures on much larger scales than individual galaxies and therefore applying both of these ‘corrections’ is justified. With these procedures, the resulting density field is cleaned from the smearing effect of the cluster-fingers, and at the same time, retains roughly constant value with the distance (Liivamagi et al. 2012), despite the falling number density of galaxies.

Luminosity densities  $\ell$  on the grid are calculated as

$$\ell(\mathbf{r}_i) = \sum_{\text{gal}} K_B^{(3)}(\mathbf{r}_{\text{gal}} - \mathbf{r}_i; a, \Delta) L_{\text{gal,w}}, \quad (1)$$

where  $\mathbf{r}_{\text{gal}}$  are the coordinates and  $L_{\text{gal,w}}$  is the weighted luminosity of a galaxy. The three-dimensional smoothing kernel  $K_B^{(3)}$  is a direct product of  $B_3$  spline functions (see Appendix A for details)

$$K_B^{(3)}(\mathbf{r}; a, \Delta) = \left(\frac{\Delta}{a}\right)^3 B_3(x/a)B_3(y/a)B_3(z/a), \quad (2)$$

$$\mathbf{r} \equiv (x, y, z).$$

Parameters  $a$  and  $\Delta$  denote smoothing scale and lattice cell length respectively. Galaxy data and resulting density field are given in a rectangular coordinate system based on the SDSS survey coordinates  $\eta$  and  $\lambda$ , and comoving distance  $d$ :

$$\begin{aligned} x &= -d \sin \lambda, \\ y &= d \cos \lambda \cos \eta, \\ z &= d \cos \lambda \sin \eta. \end{aligned} \quad (3)$$

We have chosen the grid cell length to be 1 Mpc, sufficiently smaller than the structures we are studying, resulting in a lattice with  $N = 1069 \times 890 \times 1542 = 1\,467\,074\,220$  grid points. The kernel used for smoothing has an effective radius of  $a = 12$  Mpc, which roughly corresponds to  $8 h^{-1}$  Mpc used in Liivamagi et al. (2012). Smoothing scale is essentially a free parameter, however, our chosen value roughly describes the transition scale from linear to non-linear regime in structure formation (e.g. Kolb & Turner 1990; Gorbunov & Rubakov

2011). As the grid is rectangular while the galaxy sample has a cone shape, there are many lattice points in the volume with no data. Therefore we apply a mask that closely follows the sample footprint on the plane of the sky (see Figure 1), as well as having front and back faces on set distances. For convenience we convert the luminosity densities into the units of average density  $D(\mathbf{r}) = \ell(\mathbf{r})/\bar{\ell}$ . Mean density  $\bar{\ell}$  is found as the sum of all densities in the ‘unmasked region’ divided by its volume.

The number of grid points in the unmasked region is  $N_{\text{unmasked}} = 418\,879\,964$ . This number is also the unmasked/observed volume ( $V_{\text{obs}}$ ) in the units of  $\text{Mpc}^3$ , which is the effective volume of one grid cell. Only the unmasked cells of the density field are used in analysis.

### 3 NUMBER OF SUPERCLUSTERS AND PERCOLATION

We identify the isolated regions above a given density threshold  $D_{\text{th}}$  using the friend-of-friend algorithm on the grid with the linking length of one grid cell length, i.e. linking adjacent vertices; we refer to these as ‘isolated overdense regions’. In this section we study the number of such regions ( $N_{\text{R}}$ ) and their percolation properties using volume fractions – ‘filling factor’ (FF) and ‘largest cluster statistics’ (LCS)<sup>1</sup> – which are defined as follows (Yess & Shandarin 1996; Shandarin & Yess 1998):

$$\text{FF} = \frac{\text{total volume of all the isolated overdense regions}}{\text{volume of the whole unmasked region } (= V_{\text{obs}})}, \quad (4)$$

$$\text{LCS} = \frac{\text{volume of the largest isolated overdense region}}{\text{total volume of all the isolated overdense regions}}. \quad (5)$$

To put it simply, FF and LCS measure the fraction of sample volume that is overdense, and the fraction of overdense volume covered by the largest region respectively.

In Figure 2, we plot  $N_{\text{R}}$  as a function of the density threshold  $D_{\text{th}}$ . The red curve shows all the isolated overdense regions. Naturally, an arbitrarily small isolated overdense region cannot be considered a supercluster. Therefore, in order to define superclusters, we first impose the requirement of a minimum size which is of the order of the smoothing scale (this condition is consistent with that used in Liivamagi et al. (2012); Einasto et al. (2011a)). In terms of volume, the condition translates into requiring a minimum volume of  $V_{\text{th}} \sim (a/2)^3 = 216 \text{ Mpc}^3$ , where  $a$  is the scale of the smoothing kernel. The blue curve in Figure 2 includes only the regions which have volume larger than the cutoff  $216 \text{ Mpc}^3$ .

Figure 3 shows the behaviour of the filling factor and largest cluster statistics. In the left panel, we plot the FF and LCS against the density threshold, and the right panel illustrates the relation between FF and LCS. Percolation transition can be identified as a discontinuous change in LCS while plotted against filling factor (Yess & Shandarin 1996;

<sup>1</sup> While calculating FF and LCS in this work, we simply count the grid cells inside each region instead of calculating the volume using SURFGEN2 (because counting cells in a large region would be a good measure of the actual volume while doing the cluster statistics, and the latter method is computationally expensive)

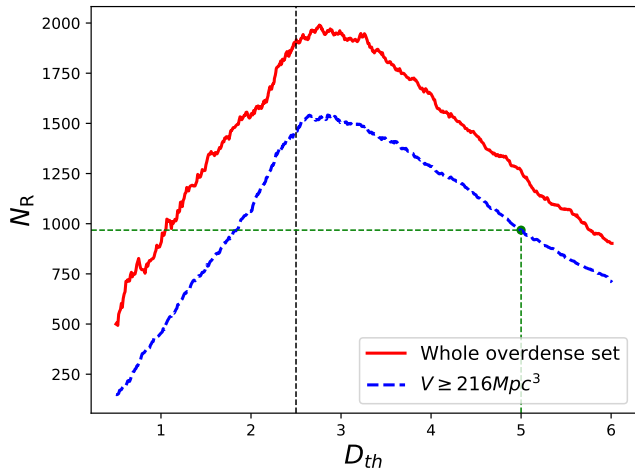


**Figure 2.** Number of isolated overdense regions ( $N_R$ ) as a function of the density threshold  $D_{th}$ . The red curve represents the case with no restriction on the minimum volume of individual regions whereas the blue curve corresponds to one where the minimum allowed supercluster volume is  $216 \text{ Mpc}^3$ . The black dashed vertical line represents the onset of percolation as explained in Figure 3. Green dot on the blue curve shows the resulting sample we get by fixing the threshold at  $D_{th} = 5.0$ , which contains  $N_R = 968$  superclusters with volume greater than  $V_{th} \geq 216 \text{ Mpc}^3$ .

Shandarin & Yess 1998); see also Einasto et al. (2018). From Figure 3, we also identify that the density field percolates at  $D \lesssim 2.5$ , which corresponds to the filling factor  $FF \gtrsim 8.6\%$ . This density threshold value at the onset of percolation coincides with the corresponding threshold found by Liivamägi et al. (2012) for the SDSS DR8 data. The percolation transition is shown by the black dashed vertical lines in Figures 2 and 3. At the percolation transition, LCS rises abruptly as we decrease  $D_{th}$  slightly while the filling factor increases slowly and smoothly. Note that the number of the isolated regions ( $N_R$ ) exhibits a peak (or a turn-around) in Figure 2 near the percolation transition for both with and without a minimum volume requirement. Percolation analysis not only helps us to understand how the connectedness of the field changes with the threshold but can also be useful to select the thresholds for defining superclusters in both fixed and adaptive threshold approaches. The critical threshold at the onset of percolation transition is important for setting the minimum threshold while finding superclusters with individual thresholds found in an adaptive approach.

We also see that imposing supercluster volume cutoff does not affect volume fractions significantly. The difference in the number of objects is in the order of several hundreds – almost a quarter, however the combined volume of those regions is negligible.

### 3.1 Selecting threshold density to define superclusters

Einasto et al. (2011a) analysed how the size and richness of superclusters in the largest nearby supercluster system, the Sloan Great Wall, change with the change of the threshold density used to define superclusters. They showed that at lower threshold density,  $D_{th} = 4.0$ , the superclusters in the

Sloan Great Wall are merged with the surrounding superclusters. As  $D_{th}$  increases, individual superclusters start to separate. At very high  $D_{th}$ , only the highest density cores of superclusters remain. Based on this analysis, Einasto et al. (2011a) suggested that the density threshold to define individual superclusters should be close to  $D_{th} = 5.0$ . Therefore, following Einasto et al. (2011a) we set  $D_{th} = 5.0$  (as shown by the green dashed vertical line in Figure 2) in order to define the superclusters for this fixed threshold approach. We obtain  $N_R = 968$  in this case with the volume cutoff  $V_{th} = 216 \text{ Mpc}^3$  (shown by the green dot on the blue curve in Figure 2). In Appendix B, we also show the results of the analysis of supercluster morphology using two other density thresholds,  $D_{th} = 4.5$  and  $D_{th} = 5.5$ .

### 3.2 Finding galaxies within superclusters

In the previous section, we studied superclusters as isolated regions with the density higher than a threshold ( $D_{th} = 5.0$ ) and volume larger than a volume cut off  $V_{th} = 216 \text{ Mpc}^3$ . Superclusters, however, are not just density enhancements, they are primarily collections of galaxies. From here onwards, we also place the galaxies inside the supercluster boundary surfaces we just determined. Additionally, we impose an extra constraint that a supercluster must have two or more galaxies in order to have an easy definition for the extent of the supercluster. This condition may reduce supercluster numbers slightly but the density level for percolation remains almost unchanged.

To assign galaxies in superclusters, we use the coordinates of the galaxies observed in the SDSS DR12 main galaxy sample (Liivamägi et al. 2012) along with the groups found on the same dataset by Tempel et al. (2017). The procedure we follow is described below.

- For each galaxy we first find out if it falls into a supercluster or not. For this purpose we check if any of the eight vertices of the cell containing a galaxy falls inside a supercluster (recall that the volume of the supercluster has to be larger than  $V_{th} = 216 \text{ Mpc}^3$ ). In such a case we assign the galaxy to that supercluster.
- If a galaxy is part of a group, we keep track of all the member galaxies of that group. If any of the member galaxies falls into a supercluster we assign all the member galaxies of the group to that particular supercluster<sup>2</sup>.
- In unlikely occasions if a group is shared by two or more superclusters we assign the whole group to the supercluster having the maximum number of member galaxies.
- Once we complete assigning all the galaxies to the superclusters, we look for the superclusters having less than two galaxies, if any at all. If such objects exist, we identify them as spurious and discard them from the final supercluster catalogue.

<sup>2</sup> Assuming that a group as a gravitationally bound object has to be either fully inside or fully outside a supercluster.

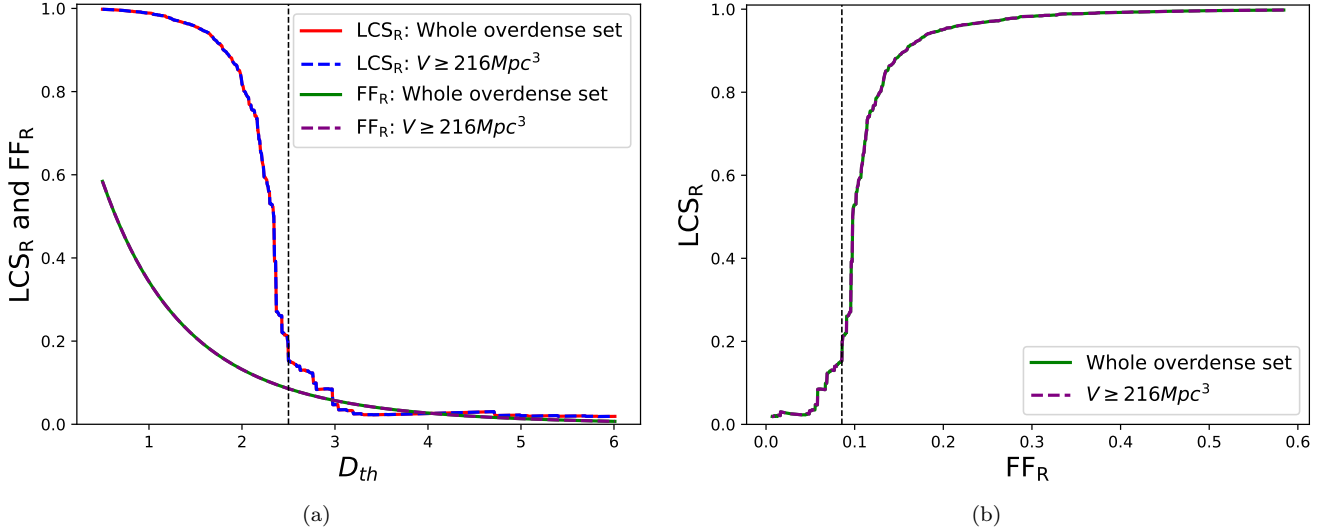


**Figure 3.** The left panel shows the filling factor (FF) and the largest cluster statistics (LCS) of the overdense volume as a function of the density threshold  $D$ . In the right panel LCS is shown as a function of FF. The solid curves in both the panels include all the regions whereas for the dashed curves we consider only the regions which have volume larger than a cutoff  $V_{\text{th}} = 216 \text{ Mpc}^3$ .

#### 4 MINKOWSKI FUNCTIONALS AND SHAPEFINDERS

The morphology of a closed two dimensional surface embedded in three dimensions is well described by the four Minkowski functionals (MFs) which are as follows (Mecke et al. 1994)

- (i) Enclosed volume:  $V$ ,
- (ii) Surface area:  $S$ ,
- (iii) Integrated mean curvature (IMC):

$$C = \frac{1}{2} \oint \left( \frac{1}{R_1} + \frac{1}{R_2} \right) dS, \quad (6)$$

- (iv) Integrated Gaussian curvature or Euler characteristic:

$$\chi = \frac{1}{2\pi} \oint \frac{1}{R_1 R_2} dS. \quad (7)$$

Here  $R_1$  and  $R_2$  are the two principal radii of curvature at any point on the surface.

The fourth MF (Euler characteristic) can be written in terms of the genus ( $G$ ) of the surface as follows,

$$G = 1 - \chi/2 \equiv (\text{no. of tunnels}) - (\text{no. of isolated surfaces}) + 1. \quad (8)$$

It is well known that  $\chi$  (equivalently  $G$ ) is a measure of the topology of the surface. For a closed isolated surface, the genus number is an integer that measures how many ‘tunnels’ (or ‘holes’) pass through the surface. In other words, an isolated surface with  $n$  tunnels will have genus  $G = n$  which is invariant under any continuous deformation of the surface. For example, a simply connected surface (such as a spherical surface or any deformation of it) has no tunnel or hole passing through it and its genus value is zero,  $G = 0$ , that represents its ‘trivial topology’. On the other hand, a doughnut and a coffee mug, both have one tunnel passing through them, therefore both have  $G = 1$ . We refer to Nakahara (2003) for a detailed review about the topology and genus and Mecke

et al. (1994) for a comprehensive discussion on applications of MFs including genus in cosmology.

The ‘Shapefinders’, introduced in Sahni et al. (1998), are ratios of the MFs, namely

$$\begin{aligned} \text{Thickness} : T &= 3V/S, \\ \text{Breadth} : B &= S/C, \\ \text{Length} : L &= C/(4\pi). \end{aligned} \quad (9)$$

Shapefinders –  $T, B, L$  – have dimension of length, and estimate the three physical extensions of an object in 3-dimensions<sup>3</sup>. The Shapefinders are spherically normalized, i.e.  $V = (4\pi/3)TBL$ .

Using the Shapefinders one can determine the morphology of an object (such as an isodensity surface), by means of the following dimensionless quantities<sup>4</sup> which characterize its

<sup>3</sup> In general one finds  $L \geq B \geq T$ . However, if the natural order  $T \leq B \leq L$  is not maintained, we choose the smallest dimension as  $T$  and the largest one as  $L$  to restore the order. In rare cases where a cluster has  $C < 0$  we shall redefine  $C \rightarrow |C|$  to ensure that  $B$  and  $L$  are positive.

<sup>4</sup> One can redefine ‘length’ by taking the genus of an object into account (Sheth et al. 2003),

$$L_1 = \frac{C}{4\pi(1 + |G|)}.$$

This reduces the filamentarity in the following manner while keeping planarity unchanged,

$$F_1 = \frac{L_1 - B}{L_1 + B}.$$

These definitions,  $L_1$  and  $F_1$ , receptively assess the ‘macroscopic’ length and filamentarity of a given object. On the other hand, the definitions of length and filamentarity, given in Eq. (9) and (11) respectively, provide us with the ‘microscopic’ information which we are interested in this work.

planarity and filamentarity (Sahni et al. 1998)

$$\text{Planarity} : P = \frac{B - T}{B + T}, \quad (10)$$

$$\text{Filamentarity} : F = \frac{L - B}{L + B}. \quad (11)$$

A simply connected spherical and a planar surface both can have same trivial topology with genus zero. However, their morphology can be easily distinguished in terms in terms of the Shapefinders, especially by the quantities  $\{P, F\}$  (both are in the range  $\in (0, 1)$ ). For a planar object (such as a sheet)  $P \gg F$ , while the reverse is true for a filament which has  $F \gg P$ . A ribbon will have  $P \sim F$  whereas  $P \simeq F \simeq 0$  for a sphere. In all cases  $0 \leq P, F \leq 1$ . Therefore, Shapefinders, together with MFs, provide us with all the information about the geometry, morphology and topology of a 3-dimensional field.

#### 4.1 SURFGEN2 algorithm

To quantify the shape of the superclusters we employ SURFGEN2, which is an advanced version of the SURFGEN algorithm originally developed by Sheth et al. (2003); Sheth (2006). The details of the refinements in SURFGEN2 can be found in Bag et al. (2019, 2018). However, for completeness, here we also briefly discuss the SURFGEN2 code which constructs isodensity surfaces from a given density field and subsequently calculates their Minkowski functionals and Shapefinders.

- SURFGEN2 code first identifies all the isolated regions above or below a given threshold in the field (e.g. a density field) within the sample volume using the friends-of-friend algorithm. Since we study galaxy superclusters in this work, we focus on the overdense part. SURFGEN2 can also find the regions consistent with periodic boundary conditions; however, it is not required in this particular work.

- Next, the code models the surface of each supercluster by triangulating the surfaces. The classic SURFGEN (Sheth et al. 2003; Sheth 2006) triangulates the surfaces using the Marching Cube algorithm (Chernyaev 1987), which has a few issues like hole formation, degeneracy etc. SURFGEN2, however, uses an improved triangulation scheme, known as ‘Marching Cube 33’ Lorenzen & Cline (1995), which circumvents the issues associated with the classic Marching Cube algorithm.

- As the last step, the MFs (and Shapefinders) are calculated for each individual supercluster using the stored triangle vertices.

Note that one could also focus on the under-dense regions in the density field and study those in the same manner.

## 5 STUDYING SUPERCLUSTER MORPHOLOGY USING SHAPEFINDERS

### 5.1 Superclusters obtained using a fixed density threshold

In this approach we define the superclusters as isolated regions which obey the following conditions.

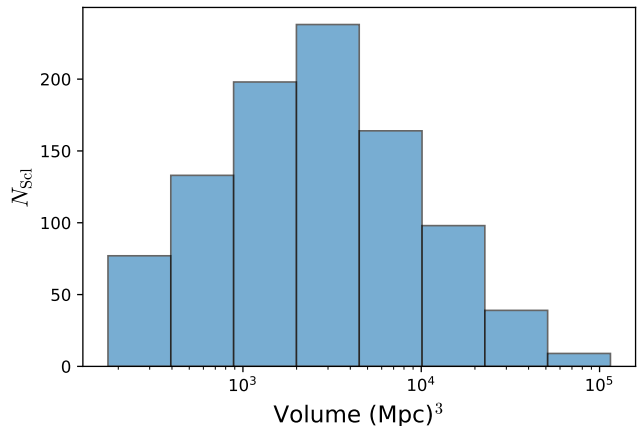


**Figure 4.** Volume distribution of superclusters for the fixed  $D_{\text{th}} = 5.0$  sample. The distribution peaks at  $\sim \mathcal{O}(10^3 \text{Mpc}^3)$ .

(i) Density has to be higher than a constant fixed threshold, i.e.,

$$D(\mathbf{r}) \geq D_{\text{th}}^C, \quad (12)$$

everywhere inside the region.

(ii) Volume of each region has to be greater than the cut-off that corresponds to a minimum size of the order of the smoothing scale, i.e.,

$$V \geq V_{\text{th}} = (a/2)^3 = (6 \text{ Mpc})^3 = 216 \text{ Mpc}^3, \quad (13)$$

where  $a = 12 \text{ Mpc}$  is our smoothing scale.

(iii) Must include two or more galaxies.

Following Liivamägi (2017); Einasto et al. (2011a); Liivamägi et al. (2012), we choose  $D_{\text{th}}^C = 5.0$  obtaining  $N_{\text{Scl}} = 956$  superclusters. The volume distribution is portrayed in Figure 4. We find most of the superclusters in the volume range  $10^3 - 10^4 \text{ Mpc}^3$ . We show the statistics of supercluster samples corresponding to a few different thresholds in Table 1, where our primary choice  $D_{\text{th}}^C = 5.0$  is highlighted in bold-face. One can notice that, as we increase the density threshold, the quantities like  $N_{\text{Scl}}$ , filling factor, fraction of galaxies inside superclusters decrease. In Appendix B, we demonstrate that large superclusters are fewer, but they dominate the total supercluster-volume. This behaviour stands valid for all thresholds.

Since the MFs (strictly speaking the first three,  $\{V, S, C\}$ ) and the Shapefinders (SFs: ‘thickness’, ‘breadth’ and ‘length’ defined in (9)) are likely to increase with the volume of the superclusters by definitions, it would be less interesting to study them for individual superclusters. Hence, in this work we primarily focus on the morphological parameters, ‘planarity’ ( $P$ ) and ‘filamentarity’ ( $F$ ), and the topology, described by genus ( $G$ ), of each individual supercluster (although we calculate the previously mentioned geometrical quantities in the intermediate steps).

In Figure 5 we show the boundary surfaces of three superclusters, as modelled by the Marching Cube 33 triangulation using SURFGEN2, in 3-dimensions along with the galaxy distribution in them. For this illustration, we chose three super-

$D_{th}$	No. of isolated overdense regions ( $N_R$ )	No. of superclusters ( $N_{ScI}$ )	Total no. of grid cells inside superclusters ( $N_{cell}$ )	Total volume estimation from SURFGEN2 ( $Mpc^3$ )	FF (%)	No. of galaxies inside superclusters ( $N_{gal}$ )	Fraction of galaxies inside superclusters ( $f_{gal}$ in %)
4.5	1143	1127	7907370	7852772.11	1.89	105111	17.985
4.9	998	988	6014295	5969329.27	1.44	87785	15.020
<b>5.0</b>	<b>968</b>	<b>956</b>	<b>5626042</b>	<b>5583108.53</b>	<b>1.34</b>	<b>83815</b>	<b>14.34</b>
5.1	939	928	5264661	5223605.97	1.26	80422	13.76
5.5	826	823	4044665	4010992.76	0.97	67786	11.60

**Table 1.** Statistics of supercluster samples extracted using different fixed thresholds. The minimum volume is  $V_{th} = 216 Mpc^3$  in all cases and, furthermore, isolated overdense regions have to include at least two galaxies (causing a slight discrepancy between  $N_{ScI}$  and  $N_R$ ). Notice that counting grid cells inside a supercluster is a good estimate of its volume (as long as the volume is quite large). As expected, the filling factor and the fraction of galaxies inside superclusters decrease as we increase the  $D_{th}$ .

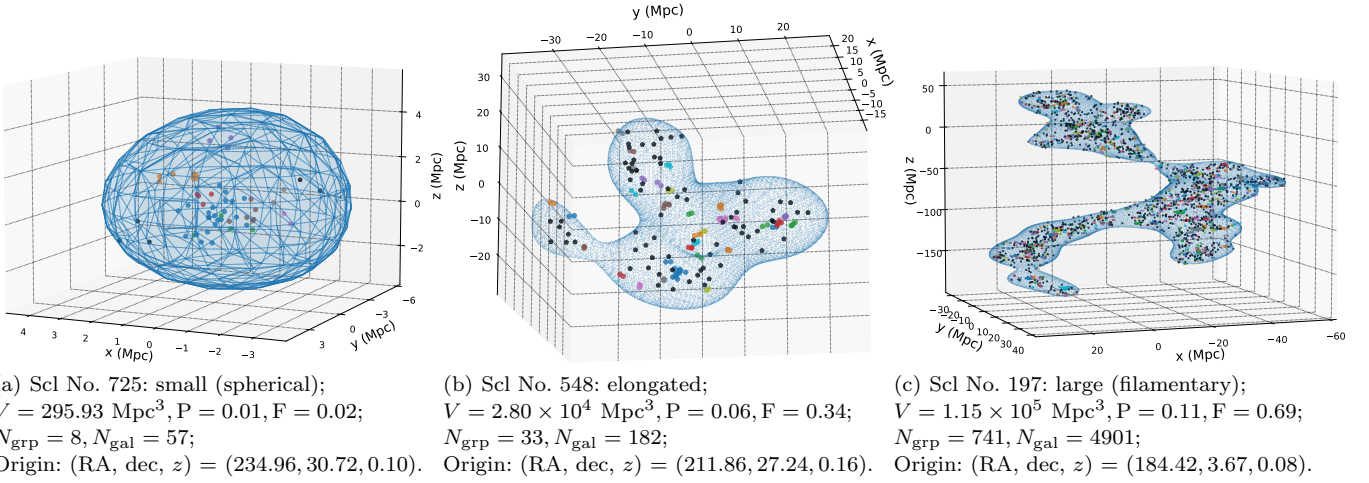


**Figure 5.** The surfaces of three superclusters – a small (left panel), a moderately large (middle panel) and the largest supercluster (right panel) – from our fixed  $D_{th} = 5.0$  catalog have been shown in 3-dimensions for demonstration. Note that only for the small supercluster in the left panel, we show the triangulated surface as modelled by SURFGEN2 whereas for the other two relatively large superclusters we depict the surface by plotting the midpoints of the triangles as there are too many in number and too small in size. All three superclusters have  $G = 0$ . We also plot the galaxy distribution inside these superclusters. Galaxies belonging to different groups are marked by filled circles with different colors whereas the lone galaxies that are not member of any group are shown by black pentagons. The origin of each plot has been shifted to the richest group inside the supercluster; the RA, dec and  $z$  of the richest group is mentioned in the respective panel caption. The panel captions also mention the size, shape of the respective superclusters as well as how many groups and galaxies they enclose. Note that ScI No. 197 given in the right most panel is identified as the richest supercluster in the Sloan Great Wall.

clusters with trivial topology ( $G = 0$ ) as examples – a small one, a moderately large one and the largest supercluster in our galaxy sample, arranged from left to right. We adopt the same Cartesian grid as in our density field but the origin in each plot has been shifted to the location of the richest galaxy group (that includes maximum number of galaxies) inside the respective supercluster. The RA, dec and  $z$  of the richest group is given in the respective panel caption which also mentions the volume ( $V$ ), planarity ( $P$ ) and filamentarity ( $F$ ) of the supercluster together with how many groups and galaxies it encloses. For the smallest supercluster, we depict the triangulated surface whereas for the larger ones we show the surface by plotting the centre of the triangles for better visualisation as there are too many triangles. We also show the galaxy distribution in each supercluster; member

galaxies of different groups are shown by different coloured circles and the lone galaxies that do not belong to any group are shown by the black pentagons. It is visually evident that the small supercluster (left panel) has quite a spherical shape that is supported by our findings of low planarity and filamentarity for this supercluster:  $P \sim 0$  and  $F \sim 0$ . The moderately large supercluster in the middle panel can be seen quite elongated and its filamentarity attains an intermediate value of  $F \approx 0.34$  while the planarity remains low,  $P \approx 0.06$ . The largest supercluster (right panel) is extremely galaxy rich as it contains 741 galaxy groups and 4901 galaxies in total. In fact, we identify this supercluster (ScI No. 197) as the richest supercluster in the Sloan Great Wall (SGW) in our cata-

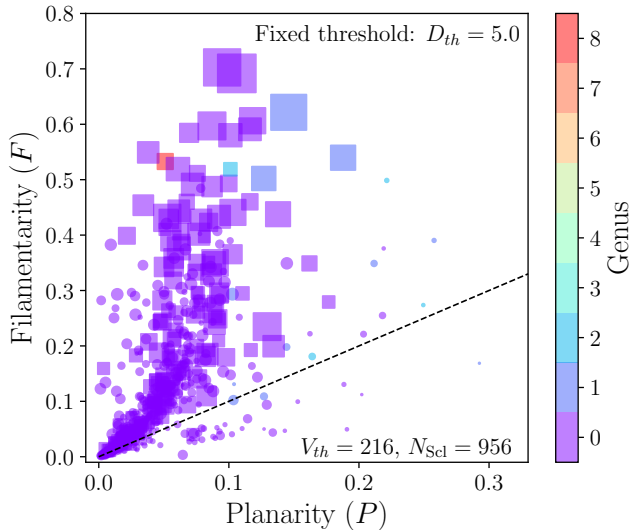


**Figure 6.** Distribution of Shapefinders in the fixed threshold supercluster sample. The smaller ( $V < 10^4 \text{ Mpc}^3$ ) and larger ( $V \geq 10^4 \text{ Mpc}^3$ ) superclusters are marked by the filled circles and squares respectively where their volumes are proportional to the size of the markers. The genus value of the superclusters is indicated by the colour bar. The dashed line represents  $F = P$  straight line above which most superclusters lie.

log (with fixed  $D_{\text{th}} = 5.0$ )<sup>5</sup>. It is visually quite filamentary, which is reflected in its high filamentarity value,  $F \approx 0.69$  and low planarity,  $P \approx 0.11$ . In all these cases, the Shapefinders, calculated using SURFGEN2, support the visual assessment.

## 5.2 Results with constant threshold

The planarity ( $P$ ) and filamentarity ( $F$ ) of individual superclusters corresponding to  $D_{\text{th}}^C = 5.0$  are shown in Figure 6 by scattered filled circles and squares for smaller ( $V < 10^4 \text{ Mpc}^3$ ) and larger ( $V \geq 10^4 \text{ Mpc}^3$ ) superclusters respectively. The limit,  $V = 10^4 \text{ Mpc}^3$ , here is roughly the same limit found in Einasto et al. (2011b) that separates large elongated superclusters from the small spherical ones. The size of the markers (circles and squares) is proportional to the volume of the superclusters. The dashed line shows the  $F = P$  straight line above which most of the superclusters lie. Genus values of the superclusters are shown by different colours. We see that smaller superclusters are more spherical, having both  $P$  and  $F$  very small. The larger superclusters are more filamentary (most large superclusters have  $F > P$ ). Although some large superclusters have slightly complex topology (genus  $G > 0$ ), most superclusters, however, have trivial topology with zero genus. Interestingly, a few outlier small superclusters are found to be quite planar or filamentary with  $G > 0$ . Figure B2 in Appendix B1 shows  $P$  and  $F$  of individual superclusters for two more thresholds  $D_{\text{th}} = \{4.5, 5.5\}$  for comparison.

In Figure 7, we plot the Shapefinders against the volume

<sup>5</sup> When we increase the flat threshold to  $D_{\text{th}} = 5.5$ , we find that Scl No. 197 breaks into several branches in our catalog.

of superclusters, divided into 8 bins. We show the volume-averaged Shapefinders in each bin (i.e. average of Shapefinders of superclusters in each bin (weighted by their volumes)). Error bars represent the standard deviation (scatter) of the respective quantities in each bin. We clearly see that smaller superclusters are mostly spherical with  $T \approx B \approx L$  (therefore,  $P \approx 0 \approx F$ ). On the other hand, as we move to the larger volume bins we find from the left panel that ‘length’ rises much more rapidly than the other two Shapefinders,  $L \gg T \approx B$ . This consequently results in steeper rise in the ‘filamentarity’ as compared to the ‘planarity’, as evident in the right panel. Therefore, the larger superclusters are quite filamentary ( $L \gg T \approx B$  which leads to  $F > P$ ). We also notice that larger superclusters tend to be slightly more multiply connected compared to the smaller ones as demonstrated by the (volume-averaged) genus curve in the right panel.

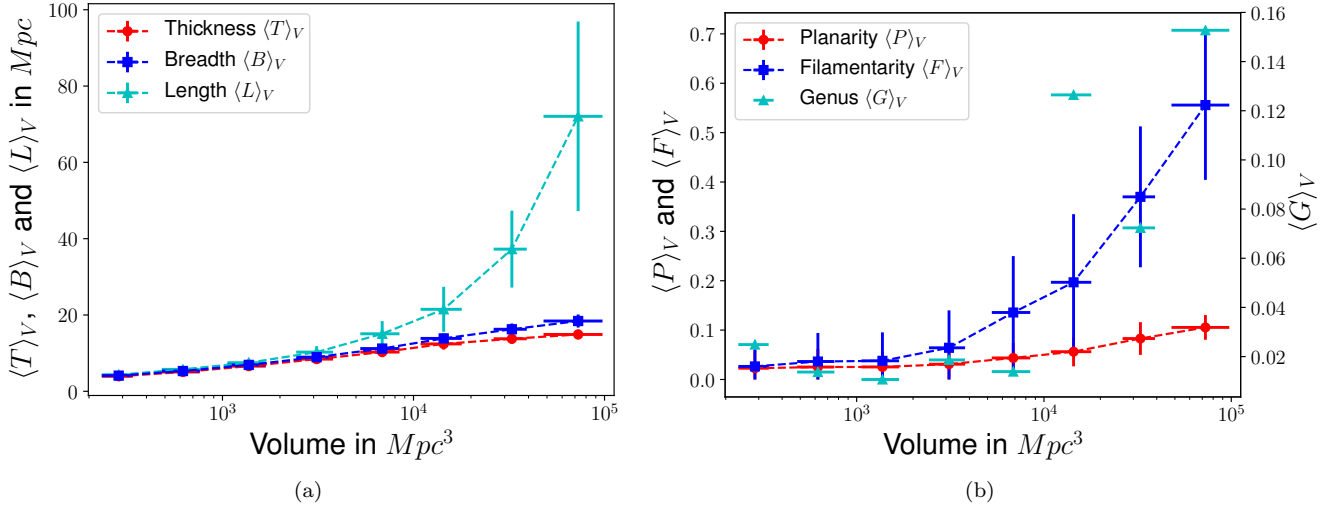
As mentioned above in the end of the Section 5.1, the largest supercluster in our catalog (with fixed  $D_{\text{th}} = 5.0$ ), Scl No. 197 (shown in the rightmost panel of Figure 5), corresponds to the Sloan Great Wall. Similarly we identify the Scl No. 651 as another famous supercluster, the Corona Borealis supercluster. We find that both these large superclusters are quite filamentary with  $(P, F) = (0.11, 0.69)$  and  $(0.10, 0.58)$  for the Scl No. 197 and 651 respectively. These numbers, as well as our overall assessments of the shape of the SGW and CB superclusters (using the SURFGEN2 algorithm) are consistent with the previous findings in the literature (Einasto et al. 2011a) based on SDSS DR7 data. The slight difference in the estimations of filamentarity between our and the analysis of Einasto et al. (2011a) can be arising from several factors, e.g. the adoption of larger smoothing scale and more refined SURFGEN2 algorithm in our work.

The statistics of superclusters having different topology shown in Figure 8. On the x-axis we plot the genus value, i.e. the number of tunnels passing through each supercluster. The blue and orange bars respectively show the fraction of superclusters having a specific genus and the fraction of supercluster-volume enclosed by them. One can notice that almost  $\sim 98\%$  of superclusters have trivial topology,  $G = 0$ , and these superclusters account for roughly 95% of the total supercluster-volume. Only a small portion of superclusters (just  $\sim 2\%$ ) have non-trivial topology,  $G \geq 1$ , and none have  $G > 2$  except the one with  $G = 8$ .

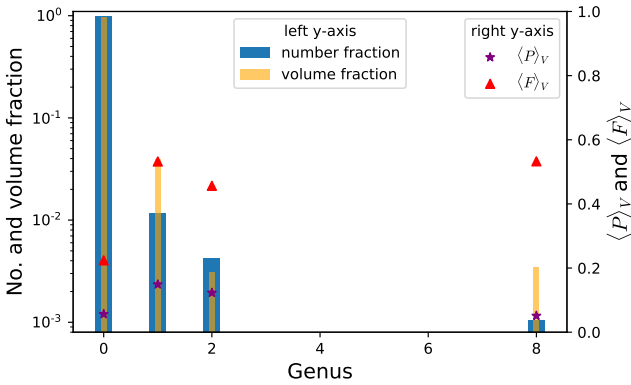
Also in Figure 8 we show the volume-averaged planarity and filamentarity, plotted along right y-axis with purple stars and red triangles respectively, for superclusters with different genus. As genus increases the volume-averaged planarity remains small,  $\langle P \rangle_V < 0.2$  but we notice a significant increase in  $\langle F \rangle_V$  among the superclusters with non-trivial topology. This clearly demonstrates that high genus superclusters tend to be significantly more filamentary.

Figure 9 shows the distribution of the shape/morphology parameters (planarity and filamentarity) of the superclusters for the three values of the threshold (the primary choice of threshold is  $D_{\text{th}} = 5$ , the other two are shown here for comparison only). The panel on the left shows the fraction of superclusters in planarity and filamentarity bins. In the right panel we plot the same but only for the large superclusters which have volume  $\geq 10^4 \text{ Mpc}^3$ . Remarkably, for different thresholds we might have different  $N_{\text{Scl}}$  (and filling factors) but the shape distributions are almost identical (especially in the left panel). We notice that superclus-





**Figure 7.** Shapefinders of the superclusters are plotted against their volume, divided into 8 bins, in the fixed threshold  $D_{th} = 5.0$  case. For each volume bin we plot the volume-averaged values of the Shapefinders: namely  $\langle T \rangle_V$ ,  $\langle B \rangle_V$ , and  $\langle L \rangle_V$  in the left panel and  $\langle P \rangle_V$ ,  $\langle F \rangle_V$ , and  $\langle G \rangle_V$  in the right panel. Error bars represent the standard deviations which show the scatter of the respective quantities in each bin (except for the genus).



**Figure 8.** Genus distribution in the constant threshold  $D_{th} = 5$  supercluster sample. Blue and orange bars represent the fraction of superclusters having different genus and the fraction of volume enclosed by those respectively (along left y-axis). Purple stars and red triangles, respectively, show the volume-averaged planarity and filamentarity of the superclusters for different genus values (plotted along the right y-axis).

ters are statistically not planar at all, more than 90% superclusters have planarity less than 0.1 in both panels. As for filamentarity, similarly, the vast majority of the objects has very small values, meaning that most have a spherical shape.

However, larger superclusters are significantly more filamentary as evident from the right panel – only around 20% of these large superclusters have  $F < 0.1$  leaving roughly 80% with  $F > 0.1$ .

Since larger superclusters tend to be more filamentary, one may prefer to study the volume weighted shape distribution. In the left panels of Figure 10, we show the fraction of supercluster volume, defined as

$$\frac{\sum(\text{Volume of superclusters falling in a } P \text{ or } F \text{ bin})}{\text{Total volume of all the superclusters}}, \quad (14)$$

falling into different planarity and filamentarity bins, again for the three density threshold values. Right panels show cumulative fraction, i.e. the fraction of the total supercluster-volume with planarity  $P > P'$  is plotted against  $P'$  (same goes for the filamentarity). We see that most of the supercluster volume is highly spherical in morphology (having both planarity and filamentarity very low) despite non-spherical superclusters typically being quite large. Considering all the superclusters, (top panels (a) and (b) in Figure 10) we find that more than 85% of the supercluster-volume has  $P < 0.1$  while only around 30 – 40% (depending on the threshold) of supercluster-volume has  $F < 0.1$  (despite having more than 70% of superclusters falling in that filamentarity bin as seen in Figure 9). For  $D_{th} = 5.0$ , 15% of supercluster-volume has  $F > 0.5$ . Focusing on the large superclusters with  $V \geq 10^4 Mpc^3$  (in bottom panels c) and (d), we again find that most of the supercluster-volume has very low planarity but now around 90% (25%) of volume of the large superclusters has  $F > 0.1$  ( $F > 0.5$ ). In contrast, the planarity distribution is almost identical across the thresholds but at a lower fixed threshold slightly larger fraction of supercluster-volume is filamentary.

Since we find a moderate variation of filamentarity (and not planarity) among the superclusters, it would be interesting to see the volume distribution of superclusters with different filamentarity. Figure 11 shows the average volume (along with the standard deviation) of the superclusters belonging to different filamentarity bins for the fixed threshold  $D_{th} = 5.0$ . It can be clearly seen that higher filamentary superclusters are statistically larger in size. This observation is consistent with that of Figure 8 and Figure B1 explained in Appendix B.

Size distribution of density field objects acquired with this approach extends to smaller dimensions. It is worth mentioning that one may doubt whether the smaller (volume) ‘superclusters’ are indeed astrophysical superclusters; some of them might be small structures like more isolated clusters or just

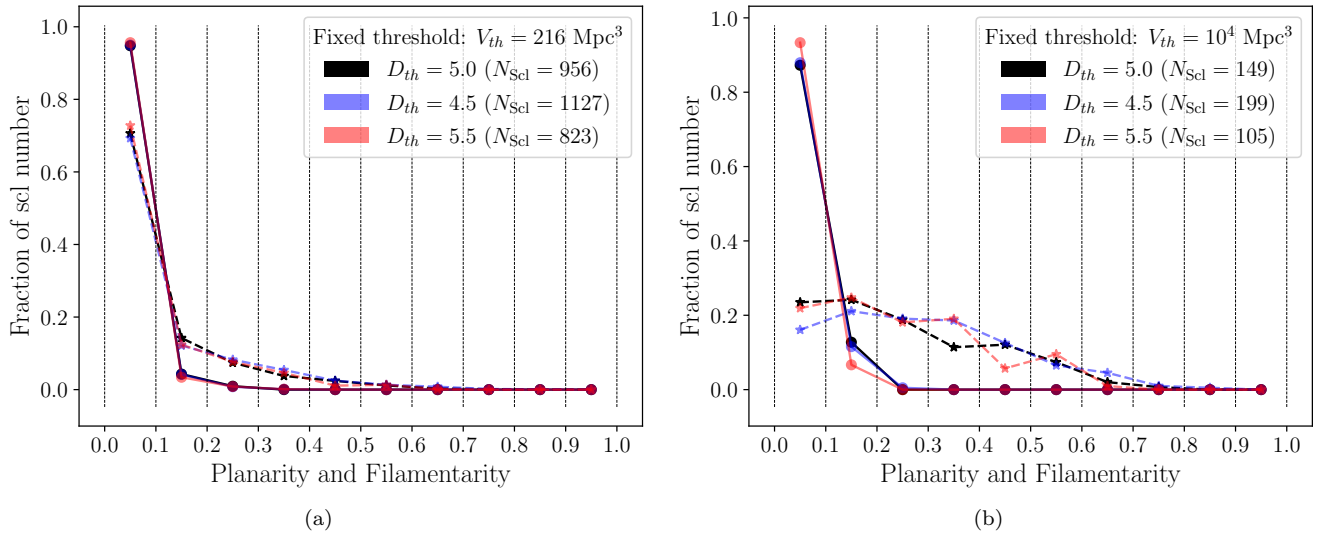


**Figure 9.** Distribution of the planarity (circles joined by solid lines) and the filamentarity (stars joined by dashed lines) of the supercluster samples extracted using different fixed density thresholds. The planarity and filamentarity ranges are divided into 10 bins. Different colours represent the results for different fixed thresholds. In the left panel we include all the superclusters whereas in the right panel we focus on the large superclusters with volume  $\geq 10^4 \text{ Mpc}^3$ .

$D_{\text{th}}^{\text{min}}$	$D_{\text{th}}^{\text{max}}$	$V_{\text{th}} (\text{Mpc}^3)$	$N_{\text{R}}$	$N_{\text{Scl}}$	FF (%)	$f_{\text{gal}}$ (%)
2.5	5.5	1728	1987	1984	4.35	31.14
2.5	6.0	1728	2005	2002	4.26	30.58
2.5	5.5	216	3249	3201	3.85	30.51
3.0	5.5	1728	1589	1587	3.49	26.80
3.0	6.0	1728	1607	1605	3.40	26.25
3.0	5.5	216	2639	2602	3.16	26.73
<b>3.5</b>	<b>5.5</b>	<b>1728</b>	<b>1271</b>	<b>1271</b>	<b>2.76</b>	<b>22.56</b>
3.5	6.0	1728	1289	1289	2.68	22.12
3.5	5.5	216	2119	2093	2.58	23.00

**Table 2.** Statistics of superclusters found with ‘adaptive’ threshold method: number of overdense regions ( $N_{\text{R}}$ ) and superclusters ( $N_{\text{Scl}}$ ), filling factor ( $FF$ ), and fraction of galaxies in superclusters ( $f_{\text{gal}}$ ) for different combinations of density threshold and volume limits  $\{D_{\text{th}}^{\text{min}}, D_{\text{th}}^{\text{max}}$  and  $V_{\text{th}}\}$ . Primary choice of the parameters is  $V_{\text{th}} = 1728 \text{ Mpc}^3$ ,  $D_{\text{th}}^{\text{min}} = 3.5$ ,  $D_{\text{th}}^{\text{max}} = 5.5$  (indicated by boldface).

random spurious density enhancements (especially on larger distances where number density of galaxies is lower). However, Appendix C demonstrates that the distribution of the geometrical properties, such as volume, weighted luminosity, morphology etc, of the superclusters remain consistent across the Universe. Therefore, these somewhat suspicious small superclusters are also homogeneously distributed in the Universe and hence do not bias our shape distribution results.

### 5.3 Adaptive density threshold case

An alternative to fixing a density threshold for all superclusters, along with a need to justify the selection of a specific one, is to try to devise a rule to find a border condition for each supercluster separately. This is akin to watershed methods used to determine large-scale voids (Platen et al. 2007; Nadathur & Hotchkiss 2014). While not as detailed in drawing structure boundaries as those mentioned, we implement an adaptive scheme to derive individual thresholds for all superclusters. Closely following Liivamägi (2017); Liivamägi et al. (2012), the adaptive threshold method is briefly described below.

- We scan the density field at multiple thresholds, spaced linearly by  $\Delta D$  in the interval  $D_{\text{th}}^{\text{min}} \leq D_{\text{th}} \leq D_{\text{th}}^{\text{max}}$ .
- Like in the fixed threshold case, we again set a minimum volume for a supercluster  $V_{\text{th}}$  which can be different from what was considered in the fixed threshold case.
- At each threshold, say  $D_{\text{th}} = D_n$ , we keep track of all the superclusters and also the threshold associated with each supercluster. Then we increase the threshold by  $\Delta D$ :  $D_{\text{th}} \rightarrow D_{n+1} = D_n + \Delta D$ .
- Suppose we see that at  $D_{\text{th}} = D_{n+1}$  a supercluster splits into multiple isolated regions. If  $N \geq 2$  of them have  $V \geq V_{\text{th}}$ , we allow the splitting and consider each of these  $N$  fragments as a separate supercluster and set their critical thresholds to  $D_{n+1}$ . Otherwise, we do not allow splitting and keep considering the larger one as a single supercluster.
- Similarly to the fixed threshold case, we impose the condition that each supercluster should include at least two galaxies, discarding them otherwise.

Superclusters found in this adaptive method depend on the choice of  $D_{\text{th}}^{\text{min}}$ ,  $D_{\text{th}}^{\text{max}}$ ,  $V_{\text{th}}$  and  $\Delta D$ . However, we observe that the method is sensitive to the choice of  $D_{\text{th}}^{\text{min}}$  and  $V_{\text{th}}$ , and very weakly dependent on  $D_{\text{th}}^{\text{max}}$  (for sufficiently large  $D_{\text{th}}^{\text{max}}$ ) and almost insensitive to  $\Delta D$  (for sufficiently small

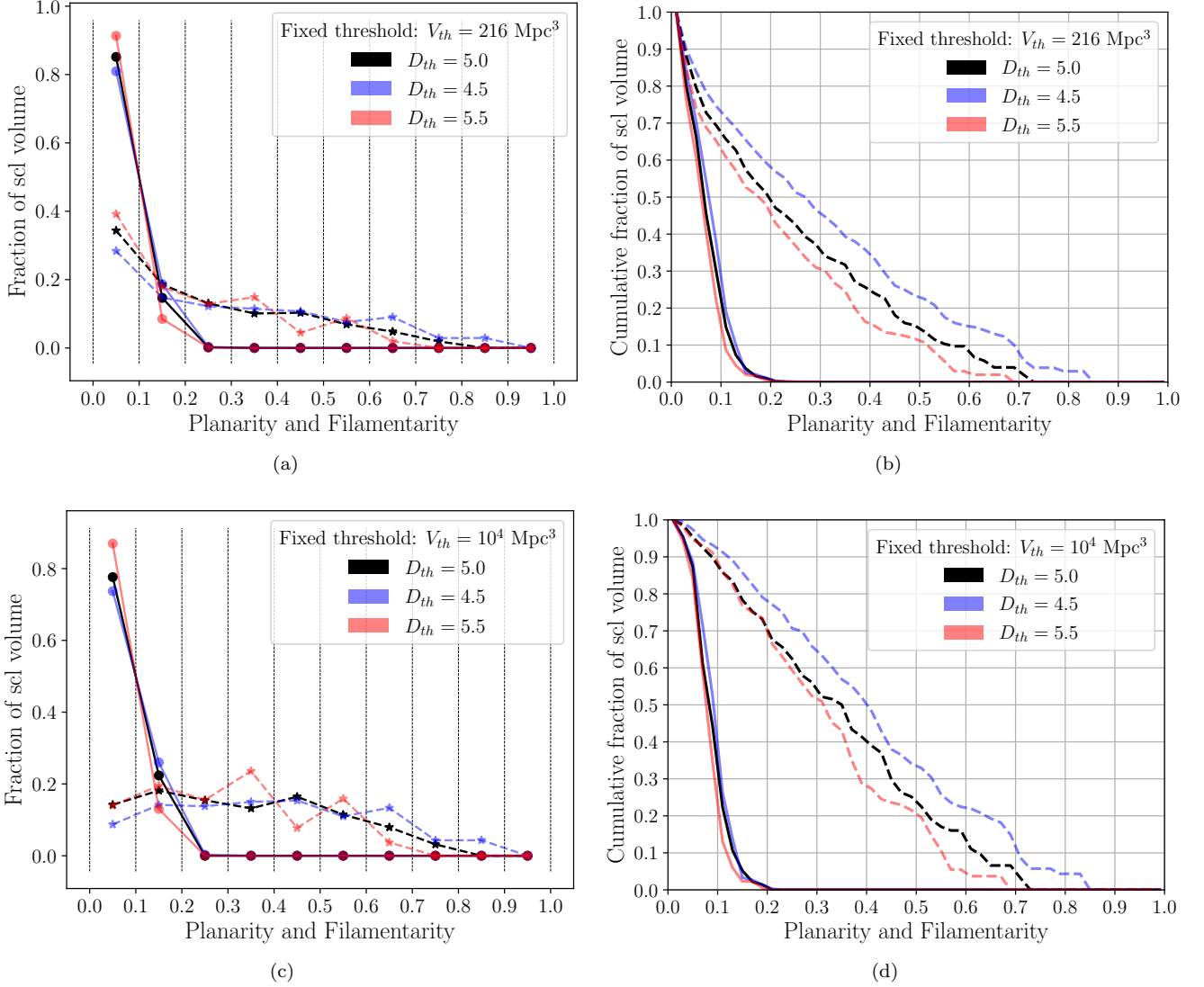


**Figure 10.** Volume weighted distributions of planarity (circles joined by solid lines) and filamentarity (stars joined by dashed lines) is depicted for supercluster samples defined using various fixed thresholds (shown by different colours). Plots in the top row contain the full supercluster samples whereas the bottom row panels include the large superclusters with  $V_{\text{th}} \geq 10^4 \text{ Mpc}^3$  only. Panels on the left, (a) and (c), show fraction of total supercluster-volume against the ‘planarity’ ( $P$ ) and ‘filamentarity’ ( $F$ ), both divided into 10 bins. In the right panels, (b) and (d), we show the cumulative fraction of supercluster-volume in different planarity and filamentarity bins. Different colours represent results for different fixed density thresholds.

$\Delta D$ ). The statistics of adaptive threshold superclusters corresponding to different choices of  $D_{\text{th}}^{\text{min}}$ ,  $D_{\text{th}}^{\text{max}}$  and  $V_{\text{th}}$  have been summarised in Table 2, some interesting details are given in Appendix D. Now we have to choose the suitable values of the parameters, most importantly  $D_{\text{th}}^{\text{min}}$  and  $V_{\text{th}}$ . Liivamägi (2017); Liivamagi et al. (2012) consider a minimum ‘diameter’ of twice the smoothing scale. However, for a more streamlined computational pipeline it will be more suitable to use a volume cutoff like in the fixed threshold case. The diameter threshold of Liivamägi (2017); Liivamagi et al. (2012) can be viewed as an equivalent of a volume cutoff at  $V_{\text{th}} = a^3 = 1728 \text{ Mpc}^3$  since the smoothing scale used in this work is  $a = 12 \text{ Mpc}$ .

Alongside, we set  $D_{\text{th}}^{\text{min}} = 3.5$ , slightly above the percolation transition which takes place at  $D_{\text{th}} \sim 2.5$ . To sum-

marise, we set  $V_{\text{th}} = 1728 \text{ Mpc}^3$  and  $D_{\text{th}}^{\text{min}} = 3.5$ ,  $D_{\text{th}}^{\text{max}} = 5.5$ ,  $\Delta D = 0.05$  in this work. This choice, which is consistent with that in Liivamägi (2017); Liivamagi et al. (2012), has been highlighted in boldface in Table 2. For this choice, the number of superclusters,  $N_{\text{Scl}} = 1271$ , is slightly larger than that in our fixed threshold case, but we have now quite large FF and  $f_{\text{gal}}$ . The volume distribution of this adaptive threshold supercluster sample has been shown in Figure 12. Note that we set the volume cutoff higher than that in the fixed threshold case. Still we find that most adaptive threshold superclusters have volume a few thousand  $\text{Mpc}^3$  which is consistent with that of the fixed threshold supercluster sample.

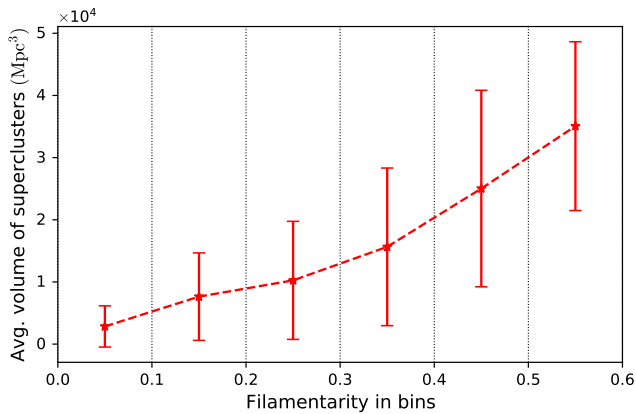


**Figure 11.** Average volume of the superclusters belonging to different filamentarity bins has been shown for the fixed threshold case ( $D_{th} = 5.0$ ). The error bars represent the standard deviation in each bin.

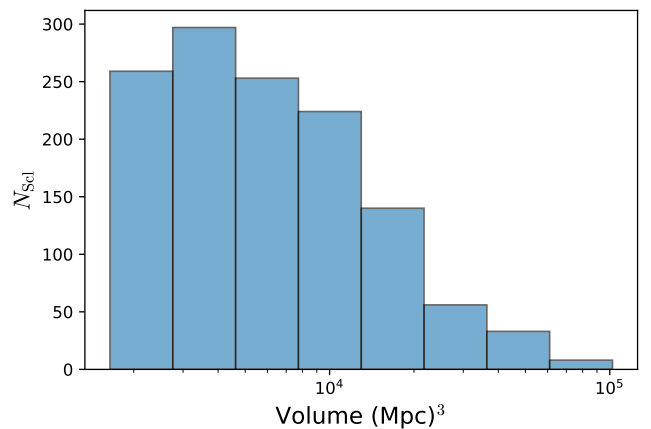
#### 5.4 Results with adaptive supercluster thresholds

The planarity ( $P$ ) and filamentarity ( $F$ ) of the individual superclusters defined in the adaptive threshold approach have been shown in Figure 13 for the parameters described above, namely  $V_{th} = 1728 \text{ Mpc}^3$  and  $D_{th}^{min} = 3.5$ ,  $D_{th}^{max} = 5.5$ ,  $\Delta D = 0.05$ . Similar to the fixed threshold case, filled circles and squares represent smaller and larger superclusters where the size of the markers is proportional to the supercluster-volumes. Comparing with Figure 6 we notice that the  $P - F$  distribution of superclusters for the adaptive threshold method is quite similar to that of the fixed threshold case. We again find that most smaller superclusters are somewhat spherical ( $P \approx 0 \approx F$ ) with zero genus while the large superclusters can be quite filamentary. Furthermore, the outliers tend to have a non-trivial topology.

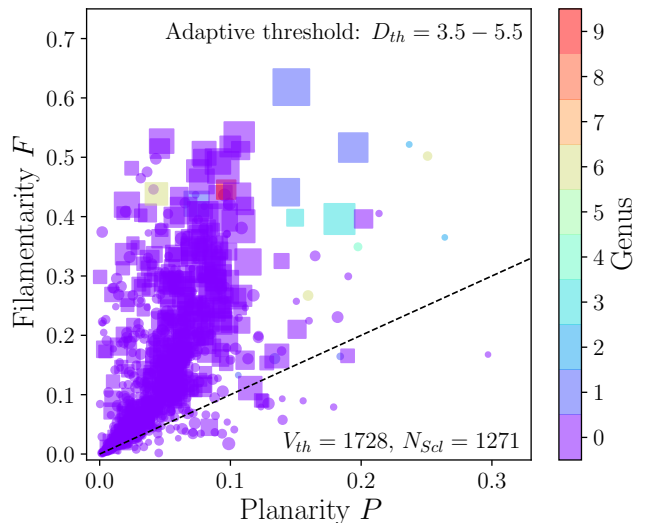
We show the dependency of the Shapefinders on the volume of superclusters in Figure 14. From the left panel, it is evident that the third Shapefinder (length) of the larger superclusters is much larger than their first two Shapefinders (breadth and thickness),  $L \gg B \sim T$ , similar to what we observe for the fixed threshold supercluster sample. This results in higher filamentarity among the large superclusters while the planarity remains small and does not increase much as we move to higher volume bins, thus  $F > P$  as shown by the right panel. Again, the (volume-averaged) genus increases with the volume and  $\langle G \rangle_V$  for large adaptive threshold superclusters is significantly higher than that for the fixed threshold case (compare the right panel with that of Figure 7).

Figure 15 shows the average volume of adaptive threshold superclusters falling into different filamentarity bins. Again, we clearly notice that higher filamentary superclusters (fewer in number) tend to be larger in size, similar to what we observe for the fixed threshold supercluster samples.

The volume weighted shape distribution of adaptive threshold superclusters is shown in Figure 16, for three different values of  $D_{th}^{min}$  (the black curves represent our primary choice,  $D_{th}^{min} = 3.5$ ). The left panel includes all the superclusters while only the large superclusters are considered in the right panel. Along the y-axes of both panels, we plot the fraction of total supercluster volume falling inside different



**Figure 12.** Volume distribution of the adaptive threshold superclusters.



**Figure 13.** Distribution of Shapefinders for adaptive threshold superclusters. The smaller ( $V < 10^4 \text{ Mpc}^3$ ) and larger ( $V \geq 10^4 \text{ Mpc}^3$ ) superclusters are marked by the filled circles and squares respectively where the size of the markers is proportional to the volume of the superclusters. The genus value of the superclusters is indicated by the colour bar. The dashed line represents  $F = P$  straight line above which most superclusters lie similar to the fixed threshold case.

planarity/filamentarity bins, as explained in Eq. (14). Remarkably, although different  $D_{th}^{min}$  results in different numbers of superclusters (and FF) but the shape distributions for them are almost identical. From the right panel it is evident that superclusters making up most of the volume have nonzero filamentarity dominated by the range  $0.1 < F < 0.2$ . More figures comparing the shape distribution of adaptive threshold superclusters are provided in Appendix D1.

Finally, we compare the shape distribution of superclusters obtained following the fixed and adaptive threshold approaches in Appendix E. Although these two distinct definitions give rise to different supercluster samples, we find that the shape distribution is very much alike.

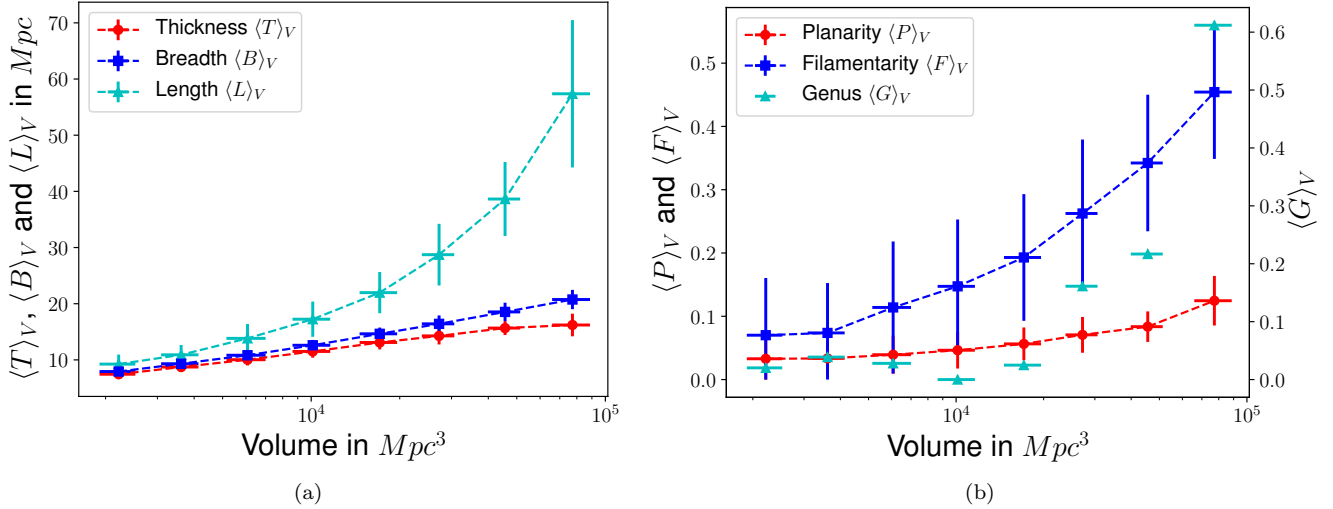


**Figure 14.** Volume-averaged Shapefinders of the superclusters with adaptive thresholds (extracted using  $\{D_{\text{th}}^{\text{min}} = 3.5, D_{\text{th}}^{\text{max}} = 5.5, V_{\text{th}} = 1728\}$ ) are plotted against the volume of the superclusters (divided into 8 bins). Genus (volume-averaged in each bin) has been plotted along the right y-axis of the right panel. The error bars represent the scatter of the respective quantities (except for genus) in each bin.

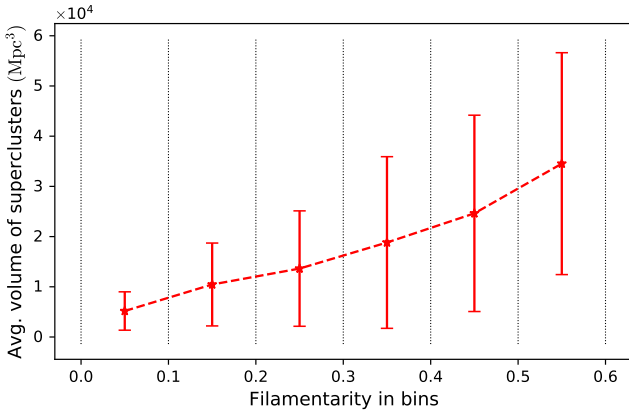


**Figure 15.** Average volume the superclusters belonging to different filamentarity bins has been shown for the adaptive threshold supercluster sample (same as Figure 11 but for the adaptive case). The error bars represent the standard deviation in each bin.

## 6 CONCLUSIONS AND DISCUSSION

Superclusters are dense and distinctive extended objects in the Universe and hence include crucial imprints of the structure formation process. Nevertheless, lacking a unique definition they are often defined according to the problem in hand. Here we study the superclusters which are extracted from a luminosity density field obtained from SDSS DR12 main galaxy sample. We construct superclusters samples separately following two definitions, namely, (i) with a fixed density threshold and (ii) with adaptive, individually assigned thresholds. After delineating the superclusters, we analyse the geometry of the individuals using the Minkowski functionals and their ratios, called Shapefinders. While Einasto et al. (2011a), Einasto et al. (2011c) have studied the morphology of individual superclusters or smaller subsamples of superclusters in the SDSS main galaxy survey (usually within

a limited redshift range), current work distinguishes itself by covering the full galaxy sample volume and more precise calculations of the Shapefinders. The important results we find from studying the morphology and shape distribution of the superclusters are highlighted below.

- Although the number and filling factor of superclusters found in these different approaches differ significantly, the morphologies are quite similar. The shape distribution we present in this article depends very little on the convention of defining the superclusters and therefore is quite robust.
- We prepare catalogues of shapes and morphology of superclusters defined in both fixed threshold and adaptive threshold methods. The catalogues are released publicly with this work (see ‘Data Availability’ section).
- We found that smaller superclusters mostly have spherical shape ( $P \approx 0 \approx F$ ) which should be influenced by the choice of the spherical smoothing filter while constructing the density field.
- However, the larger superclusters ( $V \gtrsim 10^4 \text{ Mpc}^3$ ) can be quite filamentary as well as multiply connected. Approximately 80% of these large superclusters (in both fixed and adaptive threshold samples) have  $F > 0.1$  (and roughly 40% have  $F > 0.3$ ).
- The superclusters with spherical morphology make up most of the supercluster-volume. However, if we consider only large superclusters, the total supercluster-volume is dominated by mildly filamentary structures. For example,  $\sim 88\%$  of the total volume of these large superclusters belongs to superclusters with  $F > 0.1$ . Interestingly, we find that larger volume fraction is moderately filamentary in the adaptive threshold case as compared to the fixed threshold sample where slightly bigger volume fraction falls inside the higher filamentarity bins (see Figure D4).
- The shape/morphology distributions found in this work (Figures 6, 13) are consistent with the earlier works on SDSS DR7 Liivamagi et al. (2012).

There are a lot of interesting aspects that can be pur-

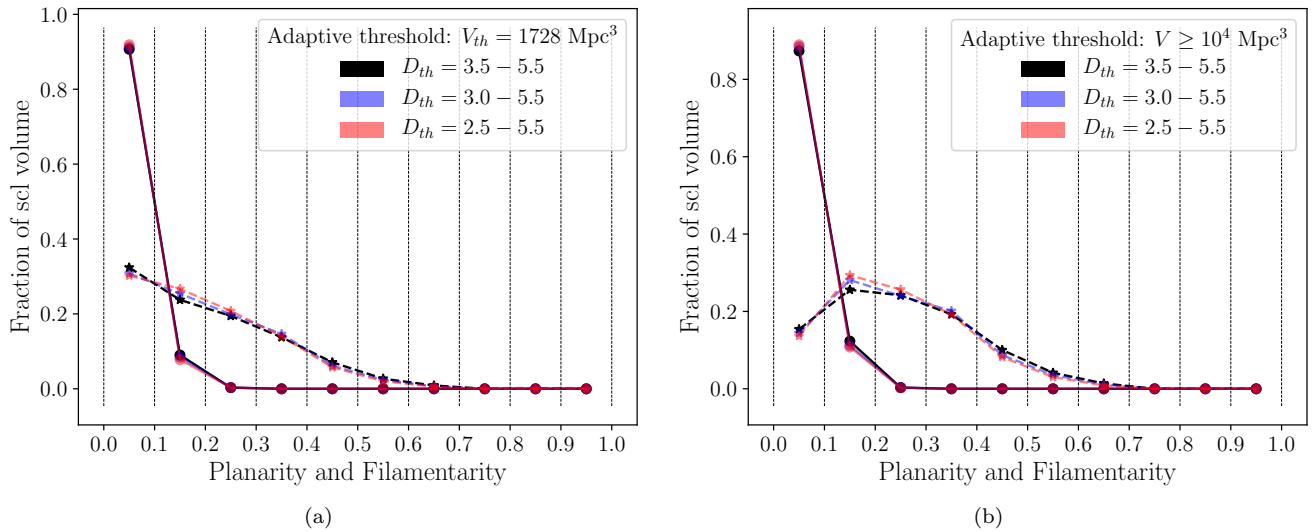


**Figure 16.** Volume weighted distributions of planarity (circles joined by solid lines) and filamentarity (stars joined by dashed lines) of all adaptive threshold superclusters is shown in the left. The right panel shows the same but only considering the large superclusters with  $V \geq 10^4 \text{Mpc}^3$ . Different colours represent various choices of  $D_{th}^{\text{min}}$ .

sued in the future. This work would allow us to shed light on the connections between the geometrical aspects of the large-scale structure and various properties related to structure formation. E.g. using the size and shape information of each supercluster one can look into the correlations between supercluster shapes/morphologies and member galaxy properties (say star formation rate, colour etc); some earlier studies attempted similar exercise on a smaller supercluster sample (Einasto et al. 2014; Cohen et al. 2017). Side by side, one can focus on the outlier superclusters in  $P - F$  diagrams and investigate how they are different from the rest. Another important future aspect of the work can be comparisons of observed structures with the ones from various large-scales simulations (based on  $\Lambda\text{CDM}$  as well as different modified gravity models) from the geometrical points of view, that can be performed using the shape distribution of the superclusters. Though, it is essential to have a consistent definition and method of extraction for superclusters for this type of exercise. Note that, similar analysis can be performed on the voids too, however, delineating voids is a less straightforward exercise.

#### ACKNOWLEDGEMENT

SB thanks Elmo Tempel for the hospitality and support during a visit to the Tartu Observatory, University of Tartu where the project was conceived and the early part of this work was done. SB also thanks Varun Sahni, Prakash Sarkar, Santanu Das for their contributions in developing SURF-GEN2 in its initial phase. We acknowledge the support by ETAG grant PRG1006 and by EU through the ERDF CoE grant TK133. We are grateful to the anonymous referee for the comments and suggestions which greatly improved the quality of this paper.

#### DATA AVAILABILITY

The SDSS DR12 data and the density field used in this article will be shared on reasonable request to the corresponding author. The supercluster shape and morphology catalogues can be accessed at [https://github.com/deltasata/Morphology\\_SDSS\\_DR12\\_scls](https://github.com/deltasata/Morphology_SDSS_DR12_scls).

#### REFERENCES

- Ahumada R., et al., 2020, *Astrophys. J. Suppl.*, **249**, 3  
 Alam S., et al., 2015, *Astrophys. J. Suppl.*, **219**, 12  
 Appleby S., Park C., Pranav P., Hong S. E., Hwang H. S., Kim J., Buchert T., 2021, arXiv:2110.06109 [astro-ph.CO]  
 Bag S., Mondal R., Sarkar P., Bharadwaj S., Sahni V., 2018, *Mon. Not. Roy. Astron. Soc.*, **477**, 1984  
 Bag S., Mondal R., Sarkar P., Bharadwaj S., Choudhury T. R., Sahni V., 2019, *Mon. Not. Roy. Astron. Soc.*, **485**, 2235  
 Bagchi J., Sankhyayan S., Sarkar P., Raychaudhury S., Jacob J., Dabhade P., 2017, *Astrophys. J.*, **844**, 25  
 Bernardeau F., Colombi S., Gaztanaga E., Scoccimarro R., 2002, *Phys. Rept.*, **367**, 1  
 Bond J. R., Kofman L., Pogosyan D., 1996, *Nature*, **380**, 603  
 Bond N. A., Strauss M. A., Cen R., 2010, *Mon. Not. Roy. Astron. Soc.*, **409**, 156  
 Chen Z., Xu Y., Wang Y., Chen X., 2019, *Astrophys. J.*, **885**, 23  
 Chernyaev E. V., 1987, *ACM SIGGRAPH Computer Graphics*, **21**, 163  
 Cohen S. A., Hickox R. C., Wegner G. A., Einasto M., Vennik J., 2017, *Astrophys. J.*, **835**, 56  
 Crofton M. W., 1868, *Phil. Trans. R. Soc. Lond*, **158**, 181  
 Davis M., Efstathiou G., Frenk C. S., White S. D. M., 1985, *Astrophys. J.*, **292**, 371  
 Davison A. C., Hinkley D. V., 1997, *Bootstrap Methods and Their Application*. Cambridge University Press, Cambridge, UK  
 Einasto J., Klypin A. A., Saar E., Shandarin S. F., 1984, *Mon. Not. Roy. Astron. Soc.*, **206**, 529  
 Einasto M., et al., 2007, *Astron. Astrophys.*, **476**, 697  
 Einasto M., Liivamägi L., Tago E., Saar E., Tempel E., Einasto J., Martinez V., Heinamäki P., 2011a, *Astron. Astrophys.*, **532**, A5

- Einasto M., Liivamägi L. J., Saar E., Einasto J., Tempel E., Tago E., Martínez V. J., 2011b, *Astron. Astrophys.*, **535**, A36
- Einasto M., et al., 2011c, *Astrophys. J.*, **736**, 51
- Einasto M., Lietzen H., Tempel E., Gramann M., Liivamägi L. J., Einasto J., 2014, *Astron. Astrophys.*, **562**, A87
- Einasto M., et al., 2015, *Astron. Astrophys.*, **580**, A69
- Einasto M., et al., 2016, *Astron. Astrophys.*, **595**, A70
- Einasto J., Suhhonenko I., Liivamägi L. J., Einasto M., 2018, *Astron. Astrophys.*, **616**, A141
- Einasto J., Suhhonenko I., Liivamägi L. J., Einasto M., 2019, *Astron. Astrophys.*, **623**, A97
- Einasto M., et al., 2020, *Astron. Astrophys.*, **641**, A172
- Einasto J., Hütsi G., Suhhonenko I., Liivamägi L. J., Einasto M., 2021a, *Astron. Astrophys.*, **647**, A17
- Einasto M., et al., 2021b, *Astron. Astrophys.*, **649**, A51
- Einasto M., et al., 2022, arXiv e-prints, p. arXiv:2204.08918
- Eisenstein D. J., et al., 2011, *Astron. J.*, **142**, 72
- Friedrich M. M., Mellema G., Alvarez M. A., Shapiro P. R., Iliev I. T., 2011, *Mon. Not. Roy. Astron. Soc.*, **413**, 1353
- Gorbunov D. S., Rubakov V. A., 2011, Introduction to the theory of the early universe: cosmological perturbations and inflationary theory. World Scientific, <https://cds.cern.ch/record/1354521>
- Gregory S. A., Thompson L. A., 1978, *Astrophys. J.*, **222**, 784
- Hikage C., et al., 2003, *Publ. Astron. Soc. Jap.*, **55**, 911
- Hikage C., Komatsu E., Matsubara T., 2006, *Astrophys. J.*, **653**, 11
- Jõeveer M., Einasto J., Tago E., 1978, *Mon. Not. Roy. Astron. Soc.*, **185**, 357
- Jasche J., Leclercq F., Wandelt B. D., 2015, *JCAP*, **01**, 036
- Kaiser N., 1987, *Mon. Not. Roy. Astron. Soc.*, **227**, 1
- Kapahtia A., Chingangbam P., Ghara R., Appleby S., Choudhury T. R., 2021, arXiv:2101.03962 [astro-ph.CO]
- Koenderink J. J., 1984, *Biological Cybernetics*, **50**, 363
- Kolb E. W., Turner M. S., 1990, The early universe. Frontiers in physics, Westview Press, [doi:10.1201/9780429492860](https://cds.cern.ch/record/206230), <https://cds.cern.ch/record/206230>
- Libeskind N. I., et al., 2018, *Mon. Not. Roy. Astron. Soc.*, **473**, 1195
- Lietzen H., et al., 2016, *Astron. Astrophys.*, **588**, L4
- Liivamägi L. J., 2017, PhD thesis, Universitatis Tartuensium
- Liivamägi L. J., Tempel E., Saar E., 2012, *Astron. Astrophys.*, **539**, A80
- Lippich M., Sánchez A. G., 2020, arXiv:2012.08529 [astro-ph.CO]
- Lorenzen W. E., Cline H. E., 1995, Technical Report CERN-CN-95-17
- Matsubara T., Kuriki S., 2020, arXiv:2011.04954 [astro-ph.CO]
- Matsubara T., Hikage C., Kuriki S., 2020, arXiv:2012.00203 [astro-ph.CO]
- Mecke K. R., Buchert T., Wagner H., 1994, *Astron. Astrophys.*, **288**, 697
- Melott A. L., 1990, *Physics Reports*, **193**, 1
- Nadathur S., Hotchkiss S., 2014, *Mon. Not. Roy. Astron. Soc.*, **440**, 1248
- Nakahara M., 2003, Geometry, topology and physics. <http://www.slac.stanford.edu/spires/find/hep/www?key=7208855>
- Novikov D., Feldman H. A., Shandarin S. F., 1999, *International Journal of Modern Physics D*, **8**, 291
- Novikov D., Schmalzing J., Mukhanov V. F., 2000, *Astron. Astrophys.*, **364**, 17
- Pathak A., Bag S., Majumdar S., Mondal R., Kamran M., Sarkar P., 2022, arXiv e-prints, p. arXiv:2202.03701
- Planck Collaboration et al., 2016, *Astron. Astrophys.*, **594**, A13
- Platen E., van de Weygaert R., Jones B. J. T., 2007, *Mon. Not. Roy. Astron. Soc.*, **380**, 551
- Pratten G., Munshi D., 2012, *Mon. Not. Roy. Astron. Soc.*, **423**, 3209
- Saar E., 2009, in V. J. Martínez, E. Saar, E. Martínez-González, & M.-J. Pons-Bordería ed., *Lecture Notes in Physics*, Berlin Springer Verlag Vol. 665, Data Analysis in Cosmology. pp 523–563, [doi:10.1007/978-3-540-44767-2\\_16](https://doi.org/10.1007/978-3-540-44767-2_16)
- Sahni V., Coles P., 1995, *Physics Reports*, **262**, 1
- Sahni V., Sathyaprakash B., Shandarin S. F., 1998, *Astrophys. J. Lett.*, **495**, L5
- Sathyaprakash B. S., Sahni V., Shandarin S. F., 1996, *Astrophys. J.*, **462**, L5
- Sathyaprakash B. S., Sahni V., Shandarin S. F., 1998, *Astrophys. J.*, **508**, 551
- Schmalzing J., Buchert T., 1997, *Astrophys. J.*, **482**, L1
- Schmalzing J., Gorski K. M., 1998, *Mon. Not. Roy. Astron. Soc.*, **297**, 355
- Schmalzing J., Kerscher M., Buchert T., 1996, *Proc. Int. Sch. Phys. Fermi*, **132**, 281
- Shandarin S. F., Yess C., 1998, *Astrophys. J.*, **505**, 12
- Shandarin S. F., Sheth J. V., Sahni V., 2004, *Mon. Not. Roy. Astron. Soc.*, **353**, 162
- Shapley H., 1930, Harvard College Observatory Bulletin, **874**, 9
- Sheth J. V., 2004, *Mon. Not. Roy. Astron. Soc.*, **354**, 332
- Sheth J. V., 2006, PhD thesis, [arXiv:astro-ph/0602433](https://arxiv.org/abs/astro-ph/0602433)
- Sheth J. V., Sahni V., Shandarin S. F., Sathyaprakash B., 2003, *Mon. Not. Roy. Astron. Soc.*, **343**, 22
- Springel V., et al., 2005, *Nature*, **435**, 629
- Springel V., Frenk C. S., White S. D. M., 2006, *Nature*, **440**, 1137
- Tempel E., et al., 2014, *Astron. Astrophys.*, **566**, A1
- Tempel E., Tuvikene T., Kipper R., Libeskind N. I., 2017, *Astron. Astrophys.*, **602**, A100
- Tully R. B., Courtois H., Hoffman Y., Pomarède D., 2014, *Nature*, **513**, 71
- Vogelez M. S., Hoyle F., Rojas R. R., Goldberg D. M., 2004, in Diaferio A., ed., *IAU Colloq. 195: Outskirts of Galaxy Clusters: Intense Life in the Suburbs*. pp 5–11 ([arXiv:astro-ph/0408583](https://arxiv.org/abs/astro-ph/0408583)), [doi:10.1017/S1743921304000043](https://doi.org/10.1017/S1743921304000043)
- Wiegand A., Eisenstein D. J., 2017, *Mon. Not. Roy. Astron. Soc.*, **467**, 3361
- Wiegand A., Buchert T., Ostermann M., 2014, *Mon. Not. Roy. Astron. Soc.*, **443**, 241
- Yess C., Shandarin S. F., 1996, *Astrophys. J.*, **465**, 2
- Yoshiura S., Shimabukuro H., Takahashi K., Matsubara T., 2017, *Mon. Not. Roy. Astron. Soc.*, **465**, 394
- Zeldovich I. B., Einasto J., Shandarin S. F., 1982, *Nature*, **300**, 407
- de Lapparent V., Geller M. J., Huchra J. P., 1986, *Astrophys. J.*, **302**, L1

## APPENDIX A: $B_3$ SPLINE SMOOTHING KERNEL

As superclusters are searched for as regions with the luminosity density over a certain threshold in a continuous volume of space, we have to convert the spatial positions of galaxies into a density field. A standard way is by a kernel sum (Davison & Hinkley 1997, sect. 8.3.2):

$$\rho(\mathbf{r}) = \frac{1}{a^3} \sum_{i=1}^N K\left(\frac{\mathbf{r} - \mathbf{r}_i}{a}\right), \quad (\text{A1})$$

where the sum is over all  $N$  data points,  $\mathbf{r}_i$  are the coordinates,  $K(\cdot)$  is the kernel, and  $a$  the smoothing scale.

The kernels  $K(\cdot)$  are required to be distributions, positive everywhere and integrating to unity; in our case,

$$\int K(\mathbf{y}) d^3y = 1. \quad (\text{A2})$$

Good kernels for calculating densities on a spatial grid are

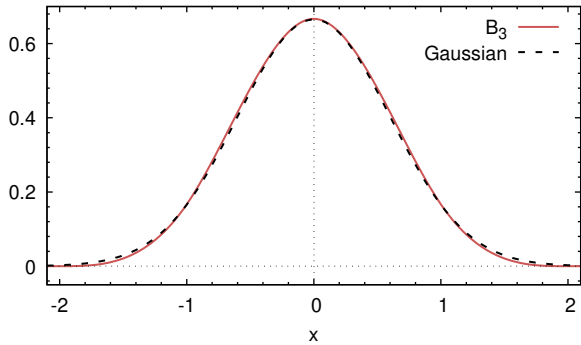


**Figure A1.** Shape of the  $B_3(x)$  spline smoothing function. Solid line – the  $B_3(x)$  kernel; dashed line – a Gaussian with  $\sigma = 0.6$ .

the box splines  $B_J$ . They are local and they are interpolating on a grid:

$$\sum_i B_J(x - i) = 1, \quad (\text{A3})$$

for any  $x$  and a small number of indices that give non-zero values for  $B_J(x)$ . To create our density fields we use the popular  $B_3$  spline function:

$$B_3(x) = \frac{|x - 2|^3 - 4|x - 1|^3 + 6|x|^3 - 4|x + 1|^3 + |x + 2|^3}{12}. \quad (\text{A4})$$

This function (shown on Figure A1 with comparison to a Gaussian) differs from zero only in the interval  $x \in (-2, 2)$ , meaning that the sum in (A3) only includes values of  $B_3(x)$  at four consecutive arguments  $x \in (-2, 2)$  that differ by 1. The three-dimensional kernel  $K_B^{(3)}$  is given by a direct product of three one-dimensional kernels:

$$K_B^{(3)}(\mathbf{r}) \equiv K_B^{(1)}(x) K_B^{(1)}(y) K_B^{(1)}(z), \quad (\text{A5})$$

where  $\mathbf{r} \equiv \{x, y, z\}$ .

Tempel et al. (2014) showed that although  $K_B^{(3)}$  is a direct product, it is very close isotropic. They also studied the properties of the density fields calculated using both  $B_3$  spline and Gaussian kernels, and found that the density values in high-density regions are practically the same. In low-density environments, however, the differences can be very large with the Gaussian smoothing strongly overestimating density, which can lead to inaccuracies when studying morphology with Minkowski functionals (Saar 2009).

## APPENDIX B: SUPERCLUSTERS FOUND WITH DIFFERENT FIXED THRESHOLDS

Supercluster statistics at different fixed thresholds have been presented in Table 1 in the main text. Note that we define the ‘fixed threshold’ superclusters subject to a critical threshold  $D_{\text{th}} = 5.0$ . However, we study the properties of superclusters defined with slightly different thresholds in this section for comparison. Furthermore, we compare the filling factor (FF) and the supercluster number ( $N_{\text{ScI}}$ ) of the large superclusters with that of all the superclusters in Figure B1. The red and green curves respectively show the ratio of filling factor and  $N_{\text{ScI}}$  between the large and all the superclusters as

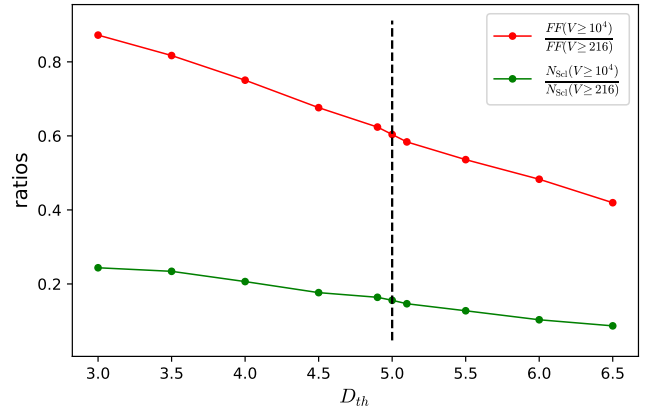


**Figure B1.** The contribution to the filling factor from the large superclusters is compared with their number fraction for different fixed thresholds around our primary choice,  $D_{\text{th}} = 5.0$  shown by the dashed vertical line. Although, a small fraction of superclusters are large but they account for most of the filling factor; e.g. at  $D_{\text{th}} = 5.0$  only  $\sim 18\%$  of the superclusters have volume larger than  $10^4 \text{Mpc}^3$  but they enclose  $\sim 65\%$  of total supercluster-volume.

functions of  $D_{\text{th}}$ . As we raise the threshold, both these ratios decrease as large superclusters become rarer. Although, a small fraction of superclusters are large but they account for most of the supercluster-volume (and hence FF) across the threshold range in the figure. For example, at  $D_{\text{th}} = 5.0$  only  $\sim 18\%$  of the superclusters have volume larger than  $10^4 \text{Mpc}^3$  but they enclose  $\sim 65\%$  of total supercluster-volume.

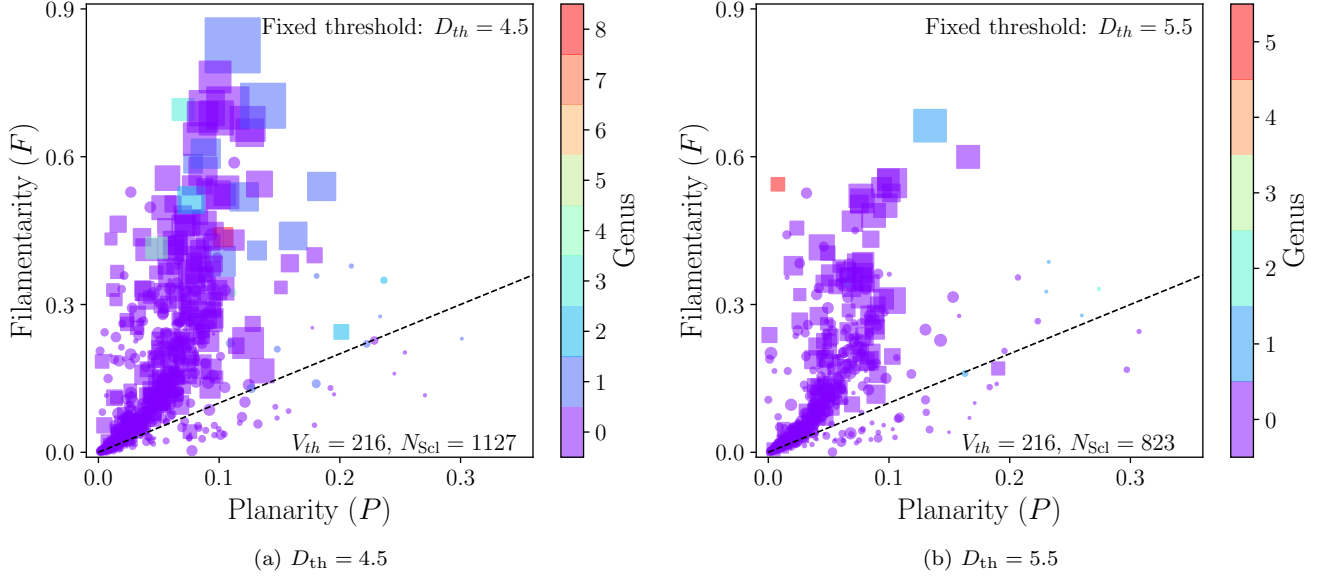
### B1 Shapefinders at different fixed thresholds

Figure 6 shows the planarity and filamentarity of individual superclusters defined with the fixed critical threshold  $D_{\text{th}} = 5.0$ . Here, we show similar plots for two slightly different thresholds,  $D_{\text{th}} = 4.5, 5.5$  in Fig. B2, for comparison. At lower threshold density ( $D_{\text{th}} = 4.5$  shown in the left panel) we obtain larger number of superclusters, in agreement with Fig. 2. Superclusters at this threshold density are larger, as they include galaxies from their surrounding regions with densities  $D_{\text{th}} = 4.5 - 5.0$ . Superclusters also tend to be more filamentary and multiply connected than superclusters obtained with the higher threshold density level ( $D_{\text{th}} = 5.5$  in the right panel). At high threshold density,  $D_{\text{th}} = 5.5$ , galaxies from outer parts of superclusters determined with  $D_{\text{th}} = 5.0$  are excluded, which decreases their filamentarity and connectivity. This explains why higher values of filamentarity and genus are found in the superclusters in the left panel as compared to the right panel. The overall pattern of the  $P - F$  distributions for slightly different fixed thresholds (comparing Figures 6 and B2) is observed to be statistically similar.

## APPENDIX C: COMPARING GEOMETRY AND SHAPES OF SUPERCLUSTERS AT DIFFERENT RADIAL DISTANCES

In this section we carry out the consistency check that whether the geometrical properties of the fixed threshold su-





**Figure B2.** Fixed threshold case: Shapefinders plots for other two values of  $D_{th}$  which can be compared with that of our primary choice,  $D_{th} = 5.0$ , shown in Figure 6. The smaller ( $V < 10^4$  Mpc<sup>3</sup>) and larger ( $V \geq 10^4$  Mpc<sup>3</sup>) superclusters are marked by the filled circles and squares respectively where the size of the markers is proportional to the volume of the superclusters. The genus value is given by the colour-bar. We again see a few outlier superclusters which tend to have non-zero genus values more often than the others. The dashed lines represent  $F = P$  straight lines above which most superclusters lie.

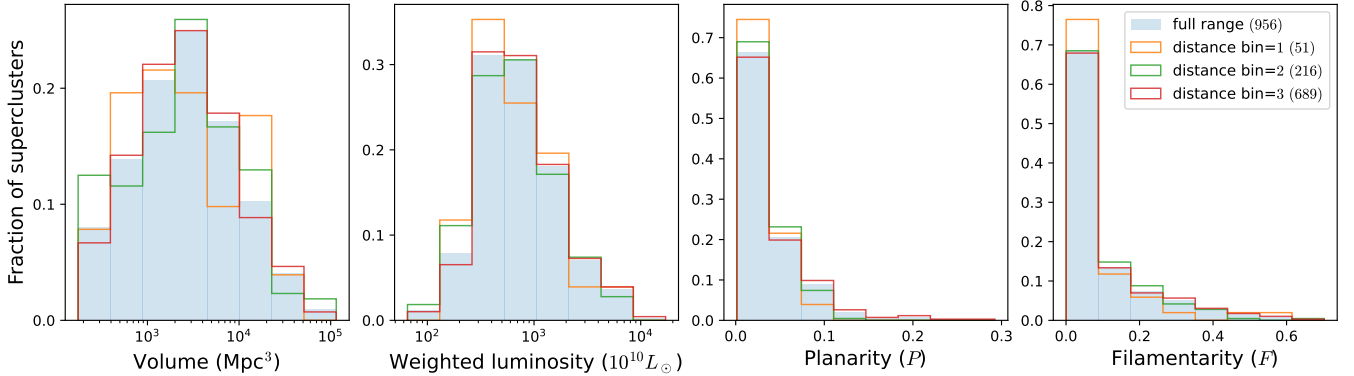


**Figure C1.** The fixed threshold supercluster sample is divided into three distance bins according to their radial distances from us. The left and right panels in the top row respectively show the volume and luminosity distributions in these the distance bins by the orange, green and red histograms. The bottom-left and bottom-right panels compare the planarity and filamentarity distributions in the superclusters belonging to the three distance bins. The number of supercluster falling to each distance bin has been shown in the parenthesis next to the bin number. The blue shaded region in all the panels represent the distribution considering all the superclusters.

perclusters remain consistent across the Universe irrespective of their distances from us. For this purpose, we divide the full supercluster sample into three bins according to their radial distances. The four panels, clockwise from the top-left, of Figure C1 compare the distributions of volume, weighted luminosity, filamentarity and planarity of these three sub-samples corresponding to three distance bins. The blue shaded histogram in all the four panels represents the full supercluster sample (the number inside the parenthesis next the distance bin number is the number of supercluster belonging to that distance bin).

It is evident from the top panels of Figure C1 that the supercluster sub-samples follow similar volume or weighted

luminosity distribution irrespective of their distances from us. However, the nearer distance bin covers smaller SDSS volume. Therefore, it is slightly more difficult to find larger superclusters in the nearby universe as evident from the fact that orange histograms in the top panels are slightly skewed towards the smaller volume/luminosity. Since we found strong correlation between the size and the shape of superclusters, the planarity and filamentarity distributions are also quite insensitive to the radial distance as illustrated in the bottom two panels. Therefore, we find that the geometrical properties of the superclusters do not vary with the radial distance from us and hence remain consistent across the Universe.

## APPENDIX D: HOW ADAPTIVE THRESHOLD SUPERCLUSTERS DEPEND ON THE CHOICE OF $V_{\text{th}}$ AND $D_{\text{th}}^{\text{min}}$

The methodology of defining superclusters with individual thresholds in the adaptive approach is briefly described in section 5.3. Supercluster sample extracted following this way is most sensitive to the choices of  $D_{\text{th}}^{\text{min}}$  and  $V_{\text{th}}$  but depends very little on reasonable choices of  $D_{\text{th}}^{\text{max}}$  and  $\Delta D$ . Some interesting facts regarding the dependencies are given below.

- When we decrease  $V_{\text{th}}$ , keeping  $D_{\text{th}}^{\text{min}}$  and  $D_{\text{th}}^{\text{max}}$  fixed, we allow more splittings. We note that a new split increases the supercluster number but decreases the filling factor (because after considering the split we also raise the individual threshold for those superclusters). But at the same time, we now allow a few smaller regions near  $D \sim D_{\text{th}}^{\text{min}}$  to be considered as superclusters which, on the other hand, raise FF slightly. This explains why  $N_C$  increases but FF (and  $N_{\text{gal}}$ ) reduces as we decrease  $V_{\text{th}}$  while keeping the other important parameters fixed. This characteristic can be observed in Table 2.

- On the other hand, if we increase  $D_{\text{th}}^{\text{max}}$  only we again permit more splittings, causing an increase in  $N_C$  but decay in FF.

- Comparing with fixed threshold superclusters: suppose in the fixed threshold case we have maximum  $N_C = n_C$  in the interval of threshold  $D_{\text{th}}^{\text{min}} \leq D \leq D_{\text{th}}^{\text{max}}$  with a  $V_{\text{th}}$ . Then in the adaptive case, we will always have  $N_C \geq n_C$  with the parameters:  $\{D_{\text{th}}^{\text{min}}, D_{\text{th}}^{\text{max}}, V_{\text{th}}\}$ .

- Raising  $D_{\text{th}}^{\text{min}}$  would significantly decrease FF, as well as  $N_C$ .

All the above findings are supported by Table 2.

### D1 Shape distributions for different $D_{\text{th}}^{\text{min}}$ in adaptive threshold approach

The Shapefinders of individual superclusters found in the adaptive threshold method has been shown in Figure 13. We show similar plots for two different choices of  $D_{\text{th}}^{\text{min}}$  in Figure D1. All these plots are again comparable to each other, we find more superclusters with lower  $D_{\text{th}}^{\text{min}}$ .

The planarity and filamentarity distributions in supercluster samples obtained in adaptive threshold method have been shown in Figure D2 for three choices of  $D_{\text{th}}^{\text{min}}$ ; the left panel includes all superclusters but the right panel focuses on the large superclusters with  $V \geq 10^4 \text{Mpc}^3$ . Remarkably, the shape distribution of superclusters corresponding to different  $D_{\text{th}}^{\text{min}}$  appears to be almost identical in both panels. The majority of the adaptive threshold superclusters have planarity smaller than 0.1. However, close to 22% of the superclusters have filamentarity higher than 0.1. Interestingly, large superclusters prefer a non-trivial morphology and the filamentarity distribution exhibits a maximum in the bin  $0.1 < F < 0.2$  as shown in the right panel. All these observations are consistent with that from Figure 16.

## APPENDIX E: COMPARING MORPHOLOGY OF SUPERCLUSTERS OBTAINED IN FIXED AND ADAPTIVE THRESHOLD METHODS

In Figure D3 we compare the shape distributions of superclusters defined in fixed and adaptive threshold methods.

The plots are already given in Figures 10 and 16, we extract the plots corresponding to our baseline thresholds in each case and compare them in Figure D3. We found no obvious difference in supercluster morphology between the two methods. However, in fixed threshold approach slightly more supercluster-volume is found in the high filamentarity bins whereas in adaptive case more supercluster-volume is in the moderate filamentarity bins. This minor difference becomes more evident when we focus on the large superclusters ( $V \geq 10^4 \text{Mpc}^3$ ) as shown in Figure D4. The planarity distributions are almost indistinguishable between the two methods.

## APPENDIX F: SUPERCLUSTERS WITH NON-TRIVIAL TOPOLOGY ( $G > 0$ )

Although most of superclusters (either in fixed or adaptive threshold catalog) have trivial topology (i.e. genus  $G = 0$ ), a handful can have non-zero genus  $G > 0$ . Figure 5 presents 3D visualisation of three superclusters with trivial topology. In this appendix, we take a closer look at the superclusters with non-trivial topology and see how galaxies are distributed in these. For simplicity, we focus on the supercluster catalog found in the fixed threshold  $D_{\text{th}} = 5.0$  approach where only 1.3% superclusters are found to have  $G > 0$ . We find that a few of these superclusters have very narrow underdense ( $D(\mathbf{r}) < D_{\text{th}}$ ) tunnels passing through them, but some have very prominent tunnels passing through them. In Figure F1, we show two such superclusters with  $G = 1$  in 3D. Similar to Figure 5, we adopt here the same Cartesian 3D grid as in our density field but shift the origin of each plot to the location of the richest group whose RA, dec and  $z$  are given in the respective panel captions. We can clearly see a prominent underdense tunnel passes through each that gives rise to their non-trivial topology. Both these superclusters include significant number of groups and galaxies as given in their panel caption which also mentions the volume, planarity, filamentarity of these superclusters. Note that member galaxies of different groups are shown with different colours and the lone galaxies are marked by black pentagons for each supercluster.

Next we turn our attention to the only supercluster that we find to have high genus number (multiply connected,  $G = 8$ ) in the fixed threshold  $D_{\text{th}} = 5.0$  catalog. It contains 11 groups and 58 galaxies in total as shown in Figure F2, the galaxies belonging to different groups are shown by filled circles with different colours and the lone galaxies are marked by filled black pentagons. Note that the eight tunnels passing through this supercluster are too narrow to be seen visually in this figure. A close inspection reveals that this particular supercluster also appears to be multiply connected with other values of fixed thresholds, and also in the adaptive threshold approach. For example, with fixed threshold  $D_{\text{th}} = 4.5$  and 5.5, this supercluster have  $G = 8$  and 5 respectively (as marked by the red square in both panels of Figure B2); its size grows with smaller  $D_{\text{th}}$  as expected. With our baseline adaptive threshold catalog, this supercluster has  $G = 9$  and it includes the same 11 groups as in the fixed  $D_{\text{th}} = 5.0$  catalog. It encloses additional 6 lone galaxies, which are marked by empty black pentagons, giving rise to  $N_{\text{gal}} = 64$  in total. The key fact that this supercluster remains multiply connected in both fixed and adaptive threshold approaches with differ-

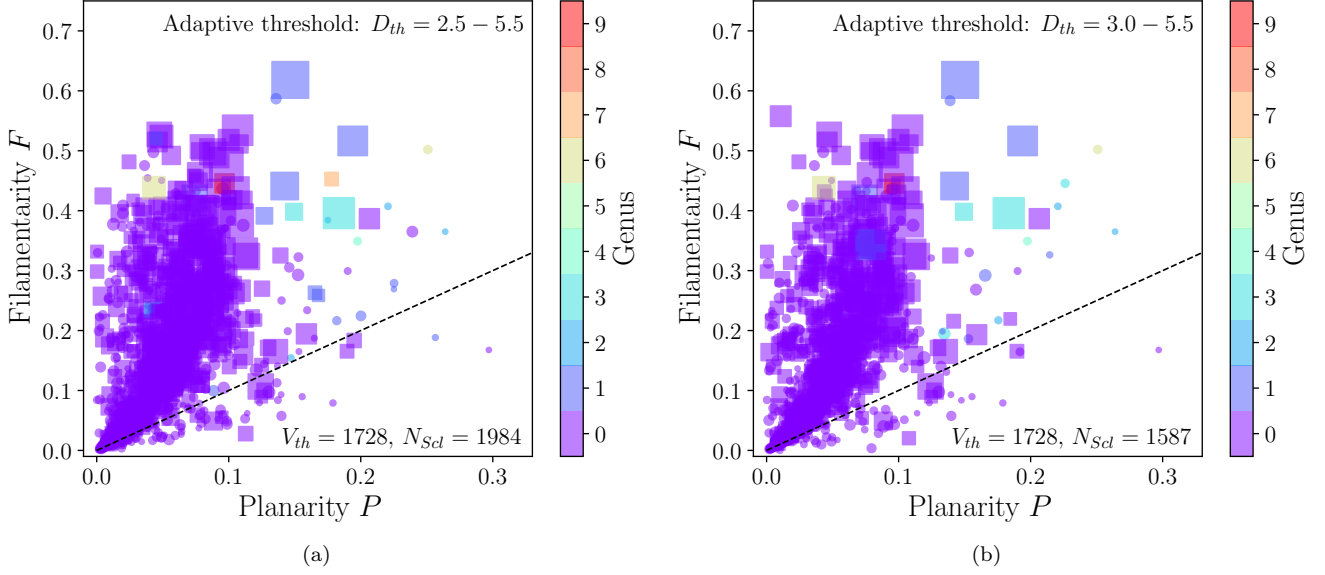


**Figure D1.** Adaptive threshold case: Shapefinders plots for two other choices of  $D_{th}^{\min}$  which can be compared with that of our primary choice,  $D_{th}^{\min} = 3.5$  (shown in Figure 13). The dashed line represents  $F = P$  straight line. The general nature of these scatter plots is visibly different (only slightly though) from the corresponding plots for fixed threshold case, compare these plots with those in Figures 6, B2.

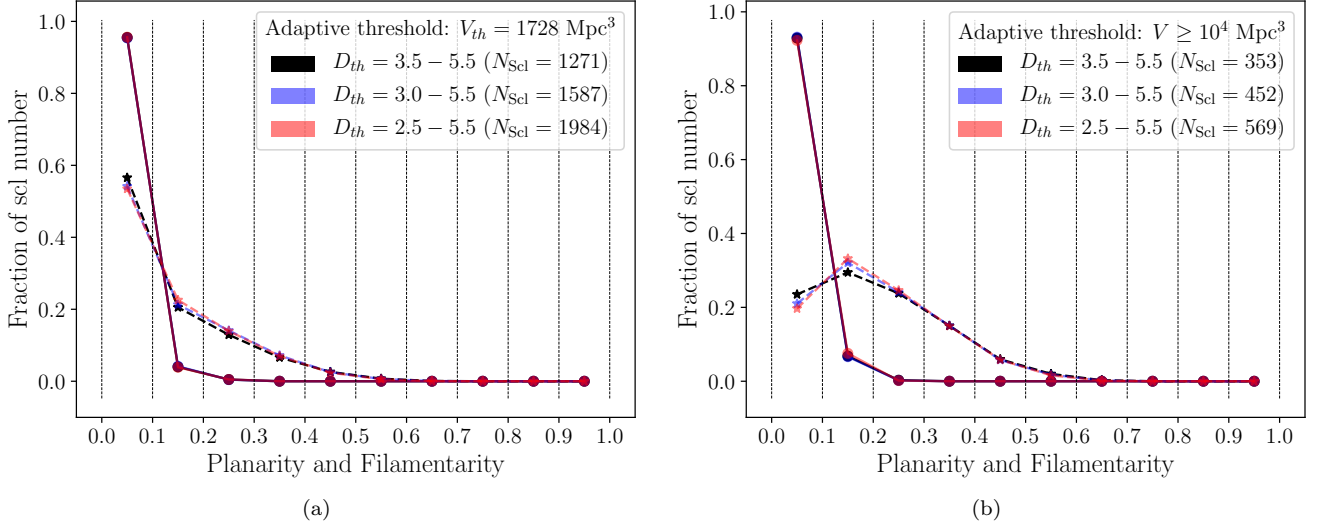


**Figure D2.** The planarity and filamentarity distributions are shown by the solid and dashed curves for the adaptive threshold supercluster samples. Different colours represent various choices of  $D_{th}^{\min}$ . The left panel contains the full supercluster samples whereas the right panel includes only the large superclusters.

ent parameter values ensures that its multi-connectedness is a robust feature for this given density field. However, since the tunnels are too narrow and this supercluster is near the boundary of the SDSS footprint, we are suspicious that the high genus number might arise due to the combination of low number of galaxies and our choice for smoothing scale. Thus we conclude that although we get a handful of superclusters with prominent tunnels (e.g. see Figure F1), for some, the non-trivial topology can be an artifact.

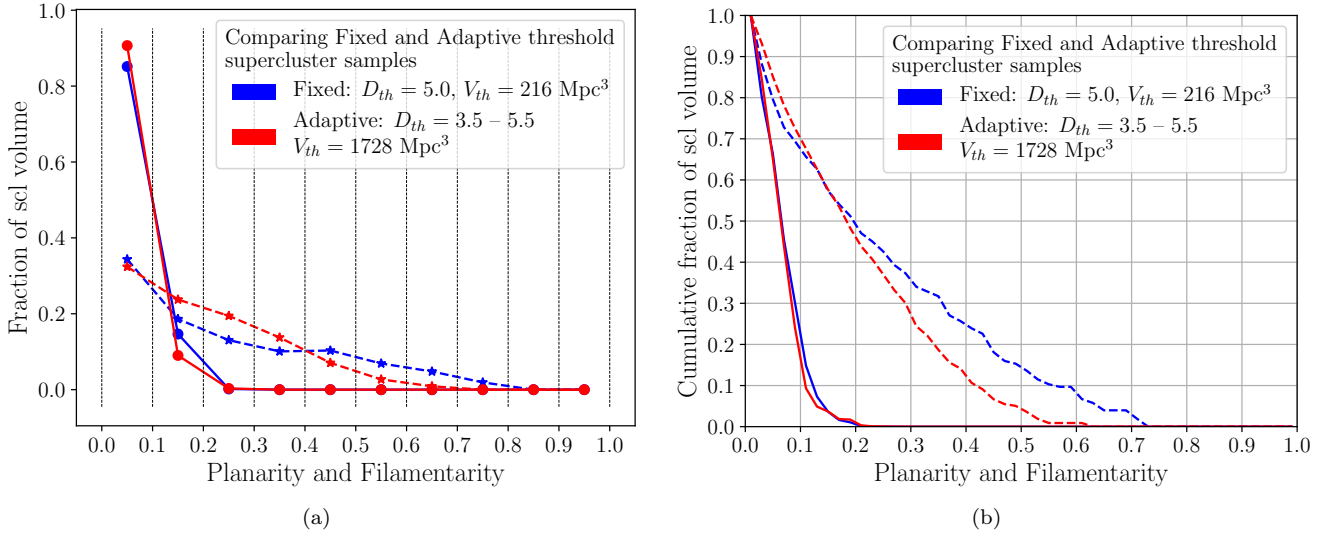


**Figure D3.** Comparing the shape distribution between the fixed threshold and the adaptive threshold supercluster samples. The solid and dashed curves represent the planarity and filamentarity distribution in both panels. The blue curves correspond to supercluster defined in the fixed threshold approach:  $D_{th} = 5.0$ . The red curves represent the adaptive threshold superclusters for the choice:  $D_{th}^{\min} = 3.5$ ,  $D_{th}^{\max} = 5.5$ ,  $V_{th} = 1728$ . We notice that the two definitions of superclusters give rise to quite similar shape distributions without any striking difference. However, in the fixed threshold case, slightly larger volume fraction falls inside the higher filamentarity bins whereas in the adaptive threshold case more volume fraction is moderately filamentary.

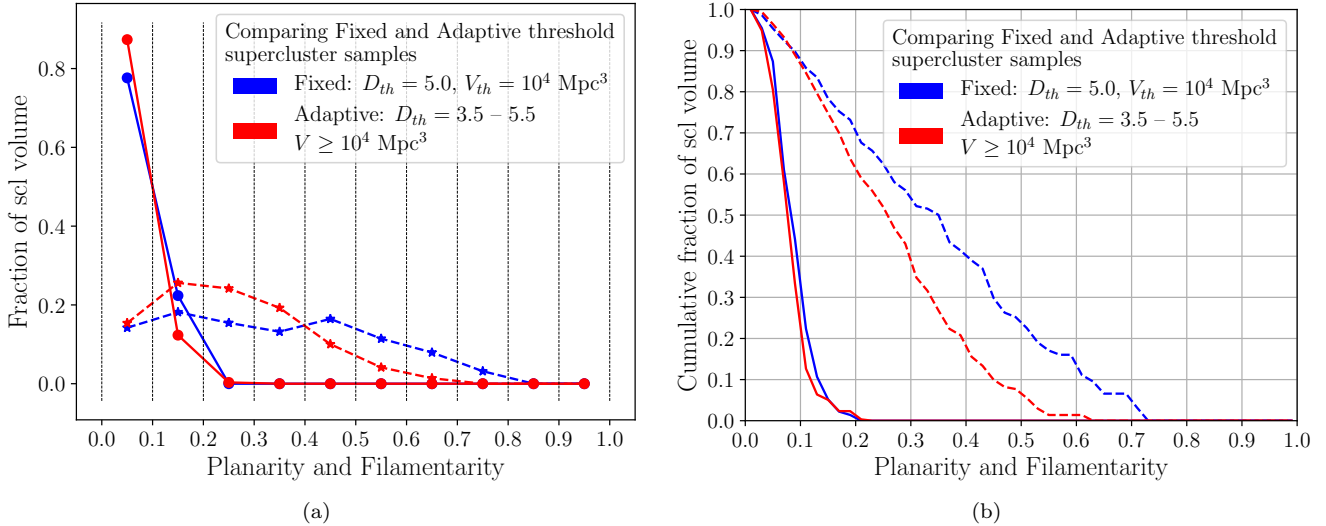


**Figure D4.** Same as Figure D3 but considering only the large superclusters with  $V \geq 10^4 \text{ Mpc}^3$ .

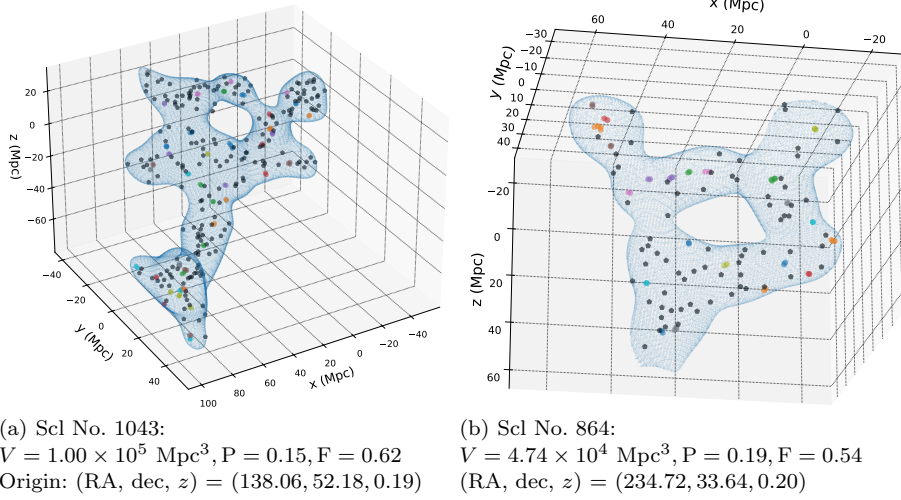


**Figure F1.** Examples of two superclusters having  $G = 1$ , i.e. one tunnel passes through each of these. The colored filled circles represent the enclosed galaxies belonging to a group whereas the lone galaxies that do not belong to any group are plotted using the black pentagons. Again, the origin is set at the location of the richest group inside each of the superclusters.

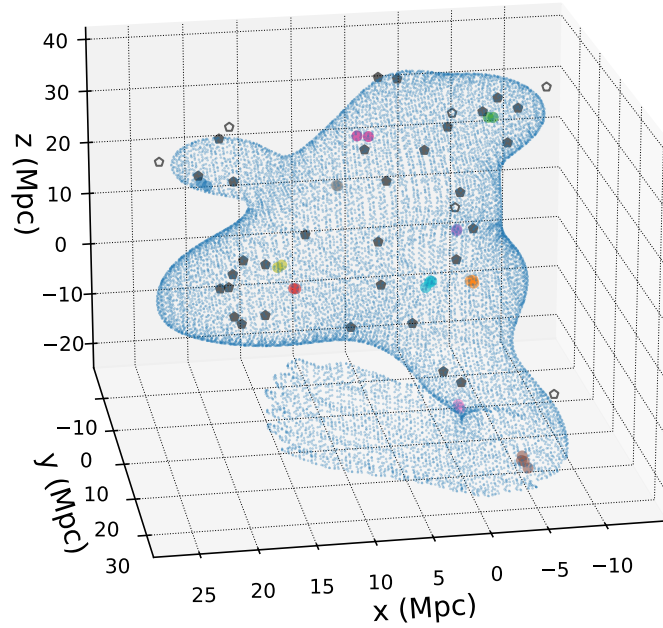


**Figure F2.** Scl No. = 251:  $G = 8$ :  $V = 1.91 \times 10^4 \text{ Mpc}^3$ ,  $P = 0.05$ ,  $F = 0.53$ . (RA, dec,  $z$ ) = (165.16, 18.07, 0.20)